Europe PMC Funders Author Manuscripts

Cryo-EM structure of the human α1β3γ2 $GABA_A$ receptor in a lipid bilayer

Duncan Laverty[1], **Rooma Desai**[2], **Tomasz Uchański**[3,4], **Simonas Masiulis**[1], **Wojciech J. Stec**[2], **Tomas Malinauskas**[5], **Jasenko Zivanov**[1], **Els Pardon**[3,4], **Jan Steyaert**[3,4], **Keith W. Miller**[2], and **A. Radu Aricescu**[1,5]

[1]MRC Laboratory of Molecular Biology, Francis Crick Avenue, Cambridge Biomedical Campus, Cambridge, United Kingdom

[2]Department of Anaesthesia, Critical Care and Pain Medicine, Massachusetts General Hospital, Harvard Medical School, Boston, Massachusetts, USA

[3]Structural Biology Brussels, Vrije Universiteit Brussel (VUB), Brussels, Belgium

[4]VIB-VUB Center for Structural Biology, VIB, Brussels, Belgium

[5]Division of Structural Biology, Wellcome Centre for Human Genetics, University of Oxford, Oxford OX3 7BN, United Kingdom

Abstract

Type A γ-aminobutyric acid receptors ($GABA_A$Rs) are pentameric ligand-gated ion channels (pLGICs) and the main drivers of fast inhibitory neurotransmission in the vertebrate nervous system1,2. Their dysfunction is implicated in a range of neurological disorders, including depression, epilepsy and schizophrenia3,4. Amongst the numerous assemblies theoretically possible, α1β2/3γ2 $GABA_A$Rs are most prevalent in the brain5. The β3 subunit plays an important role in maintaining inhibitory tone and expression of this subunit alone is sufficient to rescue inhibitory synaptic transmission in a CRISPR/Cas9 derived β1-3 triple knockout6. To date, efforts to generate accurate structural models for heteromeric $GABA_A$Rs have been hampered by the use of engineered receptors and the presence of detergents7–9. Significantly, some recent cryo-EM reconstructions report “collapsed” conformations8,9 which disagree with the prototypical

Correspondence and requests for materials should be addressed to A.R.A. (radu@mrc-lmb.cam.ac.uk), K.W.M (kwmiller@mgh.harvard.edu) or D.L (dlaverty@mrc-lmb.cam.ac.uk).

Author Contributions D.L. and A.R.A. conceived the project. D.L. carried out protein purification, collected and processed the EM data, with assistance from S.M., and built and refined the model, with assistance from A.R.A. R.D. and K.W.M. designed and analyzed the electrophysiological experiments, which were performed by R.D. T.U., E.P. and J.S. designed and generated Mb38. S.M. developed the nanodisc reconstitution protocols. T.M. performed small-molecule docking. J.Z. developed CTF refinement algorithms. W.J.S. and K.W.M. designed and analyzed the binding experiments, which were performed by W.J.S. D.L. and A.R.A. wrote the manuscript, with input from all co-authors.

Author Information Reprints and permissions information is available at www.nature.com/reprints.

The authors declare no competing interests.

Data availability. Atomic coordinates of the human α1β3γ2L $GABA_A$R in complex with Mb38 have been deposited in the Protein Data Bank (PDB accession code 6I53). The cryo-EM density maps have been deposited in the Electron Microscopy Data Bank (EMD-4411).

pLGIC, the Torpedo nicotinic acetylcholine receptor10,11, the large body of structural work on homologous homopentameric receptor variants12, and the logic of a ion channel architecture. To address this problem, here we present a high-resolution cryo-EM structure of the full-length human α1β3γ2L, a major synaptic $GABA_AR$ isoform, functionally reconstituted in lipid nanodiscs. The receptor is bound to a positive allosteric modulator megabody and in a desensitised conformation. Unexpectedly, each $GABA_AR$ pentamer harbours two phosphatidylinositol 4,5-bisphosphate (PIP2) molecules, whose head groups occupy positively-charged pockets in the intracellular juxtamembrane regions of α1-subunits. Beyond this level, the intracellular M3-M4 loops are largely disordered, possibly because interacting post-synaptic proteins were not included. This structure illustrates the molecular principles of heteromeric $GABA_A$ receptor organization and provides a reference framework for future mechanistic investigations of GABA-ergic signalling and pharmacology.

We isolated the full-length human α1β3γ2L receptor from a stable cell line13, reconstituted it into lipid nanodiscs, and solved its structure by single-particle cryo-EM (Fig. 1a-e, Extended Data Fig. 1 & 2a-b, Extended Data Table 1, Supplementary Video 1). Western blot analysis of reconstituted receptors revealed minimal proteolysis of receptor subunits (Extended Data Fig 2c). Radioligand binding assays demonstrate that the reconstituted receptor retains functional properties and allosteric interactions as expected in a membrane context13 (Fig. 1f, Extended Data Fig. 2d). The agonist, GABA, enhances binding of a benzodiazepine, [^{3}H]flunitrazepam (Extended Data Fig 2d), while allosteric interactions between extracellular (ECD) and transmembrane (TMD) domains are confirmed by enhancement of agonist, [^{3}H]muscimol, binding in the presence of the anaesthetic etomidate (Fig. 1f). The α1 subunit-specific nanobody Nb387, enlarged by fusion to the extracellular adhesin domain of *H. pylori* (HopQ) to generate the "megabody" Mb^{cHopQ}_{Nb38} (called here Mb38 for simplicity), was used to randomize $GABA_AR$ orientation in ice and facilitate particle alignment.

Three-dimensional reconstruction of the α1β3γ2L-Mb38 complex led to a cryo-EM map at 3.2 Å nominal resolution, which allowed model building for the ECD and TMD of all $GABA_AR$ subunits, and for the nanobody domain of Mb38 (Fig. 1, Extended Data Fig. 1a and d-g, Extended Data Fig. 3a-l, Supplementary Video 2). Intracellular domains (ICD), largely disordered in the absence of interacting post-synaptic proteins, could only be partially modelled (Extended Data Fig. 3m, Supplementary Video 2). The tri-heteromeric α1β3γ2L receptor has a five-fold quasi-symmetrical architecture throughout (Fig. 1d, e). The intact organization of the TMDs observed here (Fig. 1, Extended Data Fig. 3) is in marked contrast with previous EM reconstructions of $GABA_ARs$ in detergent 8,9 (Extended Data Fig. 4). Additional density, corresponding to the helical belt formed by the nanodisc MSP2N2 proteins and the enclosed lipid bilayer, surrounds the TMD (Fig. 1a, c). Unlike the complex we previously reported in the presence of excess Nb387, Mb38 was added to lower concentrations and is bound only at a single, presumably higher affinity site: the $\alpha1^+/\beta3^-$ interface in the receptor ECD (Fig. 1 a-e, Extended Data Fig. 5 and Supplementary Information).

N-linked glycans observed at the periphery of β3 (Asn80, β3-strand & Asn149, β7-strand) and γ2 (Asn208, β9-strand) subunits project into the extracellular environment (Fig. 1 a-b and d-e). In contrast, glycans linked to α1 subunits at Asn111 occupy the receptor vestibule and remain in an immature form, modelled here as $Man_4GlcNAc_2$ units (Extended Data Fig. 6a, b), as observed in other heteromeric $GABA_AR$ structures7–9. The arrangement of α1 subunit N-linked glycans likely serves to regulate receptor assembly and stoichiometry, limiting the number of α subunits per pentamer to maximum two7,8. We propose that, together with the unique properties of subunit interfaces, this ensures an ordered assembly whereby an α1β3 dimer combines with an α1β3γ2L trimer to form a hetero-pentameric receptor7,8 (Extended Data Figs. 6, 7 and Supplementary Information).

In addition to annular lipids on the extracellular side of the bilayer, modelled as POPC moieties (Extended Data Fig. 8a), we discovered distinct EM densities associated with the cytosolic side of α1 subunits within electropositively-charged pockets (Fig. 2a, b, Supplementary Videos 1 and 2). The high EM map quality allows unambiguous assignment to phosphatidylinositol 4,5-bisphosphate (PIP2) (Fig. 2a), confirmed by all our high-resolution, small molecule-bound, $GABA_AR$ structures14. The inositol 1,4,5-trisphosphate (IP3) head groups form extensive interactions with the protein backbone, as well as charged and polar residues on the α1 M3 (Lys312 and Arg313) and M4 helices (Ser388, Ser390 and Lys391; Fig 2c, d). Sequence alignment reveals strict conservation of these residues amongst α-subunits of synaptic-type $GABA_ARs$ (Fig. 2e, Extended Data Fig. 8b). The IP3 phosphate group at position 1 is also coordinated by the side chain of Arg249 protruding from the α1 M1-M2 loop (Fig. 2c, d). This loop directly affects receptor desensitization15,16 and arginine residues at this position are conserved amongst the synaptic α-subunits (α1-3,5) or replaced by lysine residues in extrasynaptic α-subunits (α4,6) (Fig. 2e).

PIP2, an important component of the inner leaflet of plasma membranes, might have two functional roles in $GABA_ARs$. First, it might directly regulate channel function17, as it does in inwardly-rectifying potassium channels18. Second, it might be involved in the internalization of synaptic, but not extrasynaptic, receptors. To test the first hypothesis, we performed inside-out patch-clamp electrophysiology on the same cell-line used in structural studies. As receptors expressed on HEK293 cells were likely pre-bound to endogenous PIP2, we assessed the effects of PIP2 depletion on currents evoked by the allosteric activator etomidate. The PIP2 scavenger poly-L-lysine (PLL)17 elicited a minor enhancement of peak currents amplitudes (Extended Data Fig. 8c, d). Previous studies, assessing the effect of PIP2 depletion on steroidal modulation of $GABA_ARs$ did not reveal a functional effect on channel gating either19. Therefore, we speculate that PIP2 plays roles in regulating receptor trafficking, rather than modulating the channel function.

The agonist GABA binds at the two interfaces between adjacent β^+ and α^- subunits (Extended Data Fig. 9a). Although our structure was solved in the absence of exogenous GABA, we observe serendipitous non-protein densities at both β^+/α^- agonist binding sites (Extended Data Fig 9b, c). Relative to competitive antagonist-bound structures14 these sites adopt compact “aromatic box” configurations, lined by side chains of Phe200 and Tyr205 from loop C on the β^+ side and Phe46 and Phe65 on the α^- side (Fig. 3a,b), as observed across pLGICs12. While we cannot reliably determine the contaminating ligand identity, we

carried out *in silico* molecular docking of GABA within these sites. The most energetically favourable pose (estimated free energy of binding -6.5 kcal/mol) reveals a binding mode coordinated primarily via hydrophilic interactions (Fig. 3a, b and Extended Data Fig. 9d). In each site, the α^- Arg67 guanidinium moiety coordinates the GABA carboxylate (Fig. 3a, b). In this pose, matching those we determined experimentally in GABA/benzodiazepine and GABA/picrotoxin α1β3γ2L complexes14, the GABA amino group forms cation-π interactions with Tyr205 (Fig. 3c, d). Substitution experiments in β2-containing receptors corroborate the importance of interactions identified by docking and their effects on GABA sensitivity20. Despite differences in detail (Fig. 3), this GABA binding mode is broadly consistent with those proposed recently for α1β1γ2 and α1β2γ2 heteromers8,9.

Superposition of complementary subunit ECDs illustrates structural distinctions between β^+/α^- (agonist) and analogous sites at other interfaces (Extended Data Fig. 9f). Loops-C at α^+/β^-, α^+/γ^- and to a lesser extent γ^+/β^- interfaces protrude marginally further into the corresponding pockets. While there is a general conservation of residue type, the loss of critical aromatic ($\beta3^+$ Phe200/α1 Ser205/γ2 Thr215) and charged/polar residues (α1- Arg67/β3 Gln64/γ2 Ala79) prevents agonist binding outside canonical β^+/α^- sites. Accordingly, docking experiments at the α^+/β^-, α^+/γ^- and γ^+/β^- interfaces found GABA binding less favoured energetically (-5.5, -5.2 and -4.8 kcal/mol, respectively; Extended Data Fig. 9e).

The α1β3γ2L TMD region is fully ordered and its 5-fold symmetry is only broken by inherent sequence variations between subunit types. This is markedly different to some truncated heteromeric $GABA_AR$ structures solved in detergent (Extended Data Fig. 4), where the pore is collapsed (Extended Data Fig. 4o-r), causing long-range receptor damage8,9. The TMD forms the ion channel and displays and electropositive ring at its cytosolic portal, a determinant of ionic selectivity in pLGICs12,21(Fig. 4a). Relative to the central vertical axis, M2 helices tilt outward by ~9-11° (Fig. 4c-d). As in the cryo-EM structures of diazepam and alprazolam-bound α1β3γ2L, $GABA_AR$ β3, chimeric GLIC-$GABA_AR$_α1 and $GABA_AR$_β3-α514,22–24, the tightest pore constriction is observed at the level of the desensitization gate (-2' Pro/Ala)15, with a radius of 1.45 Å (Fig. 4b-d). At the activation gate level, the 9' Leu side chains are rotated away from the channel lumen compared to the bicuculline-bound α1β3γ2L structure14 and the pore radius is 2.38 Å (Fig. 4 b-d). Thus, the channel structure delimits a closed, non-conducting state (given the 1.8 Å Pauling radius of a dehydrated chloride ion). The concept of distinct hydrophobic gates controlling transitions between resting, active and desensitized states has been extensively studied at $GABA_ARs$ and homologous receptors15,25,26. Here the principal impediment to the flow of ions is formed by the cytoplasmic desensitization gate, thus our structure illustrates a desensitized channel conformation.

The M1, M3 and M4 α-helices delineate binding sites for a range of compounds, including neurosteroids and general anaesthetics22,23,27. The β^+/α^- interface has been extensively studied with regard to binding and modulation by anaesthetics and alcohol2,27. Accordingly, we observe a binding cavity lined by residues identified in photolabelling studies with anaesthetic derivatives28 and by Asn285 (β3 15' M2), mutation of which strongly reduces propofol and etomidate sensitivity29 (Fig. 5a, b). Additionally, transmembrane residues

labelled by the barbiturate photolabels mTFD-MPAB or mTFD-MPP27,30 map to a cavity formed at the $\gamma2^{+}/\beta3^{-}$ interface, lined at the back by γ2 Ser280 (15' M2) (Fig. 5c, d). In contrast, the $\alpha1^{+}/\gamma2^{-}$ interface appears locked by a continuous network of interactions, primarily hydrophobic (Extended Data Fig. 6f). This is consistent with the α^{+}/γ^{-} TMD interface remaining an 'orphan site', to date, with respect to receptor pharmacology27.

While sequence analyses do not predict significant secondary structure in the ICD for $GABA_AR$ subunits, this domain is known to form a scaffold for auxiliary proteins16,31. We observed protein density extending from the intracellular ends of M3 and M4 helices, most noticeably for the α1 subunits, where we were able to model part of the post-M3 (Arg313-Val323) and pre-M4 regions (Thr385-Ser390; Extended Data Fig. 9g, h). Beyond their contribution to the PIP2 binding sites described above, the $\alpha1^{-}$ post-M3 regions extend towards the neighbouring $\beta3^{+}$ subunits where interactions between α1 Trp317, β3 Phe307 and β3 Pro311 further enhance the stability of β^{+}/α^{-} interfaces (Extended Data Fig. 9g, h).

We present here the first structure of a $GABA_AR$ in a lipid bilayer. The agonist-binding site and the ECD adopt activated conformations, while the ion channel resides in a non-conducting, desensitised state. Importantly, this structure is different to those of related $GABA_ARs$ reported recently in the presence of detergents, which appear to significantly affect inter and intra-subunit interfaces8,9. We also report an α-subunit specific interaction between the $GABA_AR$ and inner leaflet lipid PIP2, which merits a detailed investigation in follow-up studies. In a physiological context, this interaction may serve to sequester receptors to specific lipid microdomains, where receptor trafficking can be precisely regulated. This hypothesis draws parallels to the proposed coupling of the *Torpedo* nAChR and cholesterol-rich microdomains32. Our results open avenues for future functional and structural studies of $GABA_AR$ modulation by lipids and small molecules, such as anaesthetics and barbiturates, that target the transmembrane domain.

Methods

$GABA_A$ receptor expression and purification

Human α1β3γ2L receptors were expressed using a stable tetracycline-inducible HEK293 cell line13 adapted to suspension culture. The cell line was not authenticated or tested for mycoplasma contamination. Briefly the cell line comprises the full-length human α1 (Uniprot ID P14867), β3 (Uniprot ID P28472) and γ2L (Uniprot ID P18507-2; 'long' isoform) genes, each under individual antibiotic selection. For purification purposes a FLAG-tag was inserted at the N-terminus of the α1 subunit and a $(GGS)_3$GK-1D4 tag inserted at the C-terminus of the γ2L subunit. Cells were grown in suspension in Freestyle293 medium supplemented with fetal bovine serum (Invitrogen) and selection antibiotics (geneticin, hygromycin-B, zeocin and blasticidin) at 37°C and 8% CO_2. At a cell density of ~$1.5\text{-}2x10^6$ cells ml^{-1} expression was induced by addition of doxycycline and sodium butyrate (Sigma) added at 5 mM to enhance expression. Cells were harvested by centrifugation after ~36 h. Cell pellets from ~1 l of suspension culture were resuspended in 20mM HEPES pH 7,2, 300mM NaCl, 1 % (v/v) mammalian protease inhibitor cocktail (Sigma-Aldrich). For solubilization a 10% (w/v) solution of lauryl maltose neopentyl glycol (LMNG, Anatrace) and cholesterol hemisuccinate (CHS, Anatrace) was prepared at 10:1

molar ratio respectively, and added at 1% (v/v) to the cell suspension. Cells were solubilized for ~1.5 h at 4°C and cell debris and insoluble material removed by centrifugation (10,000 g, 30 min). The supernatant was incubated with 1D4 affinity resin22 with gentle mixing at 4°C for ~2 h. Resin was recovered by centrifugation and washed extensively with buffer (20mM HEPES pH7.2, 300mM NaCl) containing 0.1% (v/v) LMNG before on-bead reconstitution into nanodiscs.

Nanodisc reconstitution

MSP2N2 (Addgene, ID 29520) was expressed and purified from *E. coli* as previously described33. Owing to the tendency for detergent purified receptors to aggregate upon elution, α1β3γ2L receptors were incorporated into nanodiscs while attached to 1D4 resin. Briefly, receptors attached to 1D4 resin were mixed with ~1 bed volume of buffer containing phosphatidylcholine (POPC, Avanti; prepared as a 10mg/ml stock in 3% n-dodecyl-β-D-maltoside, DDM, Anatrace – POPC final concentration ~1.2mM) supplemented with bovine brain extract (Sigma-Aldrich – Type I,Folch Fraction I; prepared as a 20mg/ml stock in 3% DDM) at 4°C for ~0.5 h. Lipids were added at a relative ratio of 85:15% POPC:brain extract. Excess lipids were removed by centrifugation before addition of an excess of MSP2N2 (~0.6mg/ml final concentration) to the receptor-bound resin-lipid mixture. The mixture of receptor-bound resin and MSP2N2 were pre-mixed gently at 4°C for ~0.5 h before addition of bio-beads SM2 (~60mg/ml; Bio-rad) to initiate reconstitution. At this point the mixture was incubated at 4°C for ~4 h with constant rotation. The resin/bio-bead mixture was recovered by centrifugation and washed extensively to remove empty nanodiscs; first with 20mM HEPES pH7.2, 300mM NaCl, next with 10mM HEPES pH7.2, 150mM NaCl and finally 10mM HEPES pH7.2, 100mM NaCl. Bound receptor-nanodisc complexes were eluted by addition of 1mM 1D4-peptide in final wash buffer at 4°C for ~16 h. The mixture was applied to EconoPac column (Bio-rad) to remove bio-beads and resin, the receptor-nanodisc complex transferred to 100 kDa Amicon Ultra concentrator (Millipore) and concentrated to 0.5 mg/ml for cryo-EM grid preparation. Sample monodispersity was assessed by analytical Size Exclusion Chromatography on a Shimadzu HPLC system and negative-stain EM. On the basis of this analysis, further purification of the sample before grid preparation was not required. Western blot analysis of cell lysates and purified receptors was performed using the following primary antibodies; rabbit anti-$GABA_A$ α1 (Millipore; 06-868), mouse anti-$GABA_A$ β2/3 (Millipore; MAB341) and mouse anti-$GABA_A$ γ2 (Synaptic Systems; 224003). Immunoreactivity was detected with secondary antibodies conjugated to horseradish peroxidase.

Generation of Mb38

Megabodies (Mbs) are rigid antibody chimeras, built from nanobodies (Nbs) that are grafted onto large scaffold proteins (examples and detailed descriptions of which are to be published in a dedicated methods paper). The particular construct used here, Mb^{cHopQ}_{Nb38} (called Mb38 throughout the text for simplicity), is a circular permutant of the extracellular adhesin domain of *H. pylori* (HopQ, UniProt B5Z8H1)34 which was inserted into the first β-turn connecting β-strands A and B of Nb387. Specifically, the Mb38 open reading frame contains the DsbA leader sequence, followed by a consensus sequence encoding the conserved β-

strand A of the Nanobody fold (residues 1-13), followed by the C-terminal part of HopQ (residues 227-449), followed by a three-residues linker connecting the C and the N-termini of HopQ, followed by the N-terminal part of HopQ (residues 49-221). The construct has C-terminal His6 and EPEA tags in frame for affinity purification. Mb38 is monomeric, with a molecular weight of ~58 kDa. Similar to Nbs, Mb38 was expressed as a secreted protein in the periplasm of *E. coli* WK6 bacteria and purified using nickel affinity chromatography followed by size-exclusion chromatography on a Superdex 200 16/60 column (GE Healthcare) in 10 mM Tris, pH 7.3,140 mM NaCl. The stock solutions were concentrated to 15 mg/mL, snap-frozen in liquid nitrogen and stored at -80°C.

Cryo-EM sample preparation

Purified α1β3γ2L-nanodisc complexes at 0.5mg/ml were mixed with Mb38 (at 1.2μM) and incubated on ice for 0.5 h prior to cryo-EM grid preparation. 3.5 microlitres of sample was applied to glow-discharged gold R1.2/1.3 300 mesh UltraAuFoil grids (Quantifoil) before blotting for 5 s at ~100% humidity and 14°C, and then plunge-frozen in to liquid ethane using a Vitrobot Mark IV (FEI).

Cryo-EM image collection and processing

Data from a single grid was collected over two 24 h sessions on a FEI Titan Krios (ThermoFisher) operated at 300kV and equipped with a Falcon 3EC direct-detector and Volta phase plate. A total of 784 micrographs were collected in electron-counting mode at a nominal magnification of 75,000 corresponding to a calibrated pixel size of 1.07Å. Each micrograph was collected as a 60 s exposure, comprised of 75 movie frames at a dose rate of 0.55e^-/p/s for a total accumulated dose of 30.84 $e^-/Å^2$. Drift correction, beam induced motion and dose-weighting were performed with MotionCor235 using a 5 x 5 patch. CTF fitting and phase shift estimation were performed on motion corrected sums without dose weighting with Gctf-v.1.1836. Micrographs were manually checked and a total of 737 micrographs (motion corrected sums with dose weighting) used for all other image processing. An initial round of auto-picking on small subset of micrographs was performed in RELION 2.137 using a Gaussian blob as a template. Picked particles were subjected to reference-free 2D classification and good classes used for auto-picking on the entire dataset. Autopicked particles were manually inspected and false positives removed, resulting in a total of 370,757 particles. Particles were 2 x binned (pixel size 2.14 Å) for initial processing. Two rounds of 2D classification were carried out in RELION 2.1 and 197,673 particles within classes exhibiting recognizable $GABA_AR$ channel features selected for further processing. An initial 3D reference model was generated in RELION and low-pass filtered to 50Å. 3D classification into six classes resulted in four good classes (106,039 particles) and two classes comprised principally of top and bottom views of the receptor-Mb38 complex. Particles from the four best classes were combined, re-extracted (1.07 Å pixel) and refined in RELION 2.1. Particle polishing (RELION 2.1) and CTF-Refine (RELION 3.0) further improved the resolution of the initial reconstruction. A second round of 3D classification, with no image alignment, yielded a single class containing 55,449 particles. 3D refinement of this class yielded a reconstruction at 3.75 Å before post-processing. Applying a soft mask in RELION Post-processing, yielded a final EM map of 3.22 Å. Notably, the calculated soft mask also accounted for density contributed by the nanodisc.

Resolution was estimated using Fourier Shell Correlation (FSC) = 0.143 criterion. Local resolution was calculated using the MonoRes implementation in Scipion38,39.

Model building, refinement and validation

An initial rigid body fit of coordinates for the truncated α1β3γ2 was carried out using UCSF Chimera40. Owing to the improved resolution of the reconstruction and apparent stability of the receptor complex in the nanodisc, a complete model of the receptor, incorporating nearly all residue side chains, could be built with high accuracy in local geometry. The model was first manually adjusted and refined using COOT41 and then subjected to global refinement and minimization in real space using PHENIX ('phenix.real_space_refine')42. Geometric constraints for lipids were generated using GradeServer (Global Phasing Ltd.) and the ligand coordinates docked into densities and refined using COOT41.

The ECD and TMD regions in all subunits were well resolved in EM density map, as were the Mb38 and N-linked glycans. However, the HopQ scaffold protein fused to Mb38 was comparatively flexible, with no apparent EM density in the final reconstruction. While density contributed by the nanodisc was evident in the EM reconstruction, the resolution did not permit modelling of the helical belt formed by MSP2N2 scaffold proteins. The final construction allowed for unambiguous assignment of α1, β3 and γ2 subunits and main-chain and sidechain model building. Strong density was observed protruding from the "intracellular" side of the nanodisc proximal to the α1 subunit TM3 and TM4 helices. We modelled this as ~10 residues of the M3-M4 loop of the α1 subunit. Strong density, unaccounted for by the protein backbone, was also apparent at the base of α1 TM3 and M4 helices. This was modelled as PIP2 on the basis of its characteristic shape and orientation at the inner leaflet of the lipid bilayer. Additional density in the "extracellular" layer of the nanodisc was modelled as POPC moieties. Cryo-EM map densities observed within the ion channel and in the (pseudo-)agonist sites were not modelled as we could not reliably determine the identity of a bound ligand.

During model building and refinement, model geometry was assessed using MolProbity43. For cross-validations, the final model was refined against the half maps generated by 3D auto-refine in RELION. Subunit interfaces and associated free energies were analysed using the PDBePISA server44. Pore diameters were calculated using the HOLE implementation in COOT. Structural figures were made using UCSF Chimera40 and Pymol (Schrodinger, LLC), including the APBS45 electrostatics plugin. Structural alignments were performed using the Superpose command in CCP4mg46 or MatchMaker40. Tunnel radii calculations were carried out using the Caver plugin47 in Pymol.

Density maps shown in figures were contoured at the following levels. Fig. 1, sharpened maps for the receptor and glycans contoured at 0.03 and unsharpened map contoured at 0.02. Fig. 6b density around PIP2 at 0.021. Extended Data Fig. 2a-c, subunits, density maps contoured at 0.03; d, e, glycans, density maps contoured at 0.025; f-h, loop C, density maps contoured at 0.03; i-k, TM helices, density maps contoured at 0.03; l density maps contoured at 0.03. Extended Data Fig. 3b, glycan, density maps contoured at 0.025. Extended data Fig. 7b, density map contoured at 0.045. Extended Data Fig. 9a, b density map contoured at 0.02.

Computational docking

Computational docking of small molecules to $GABA_AR$ cryo-EM structures was performed using AutoDock Vina48. Structures of small molecules were optimised using Grade webserver (Global Phasing Ltd.). $GABA_AR$ was kept rigid during docking. The whole agonist-binding pocket (~20×20×20 $Å^3$) centered under loop-C was selected for docking.

Electrophysiology

HEK 293 cells stably transfected with tetracycline inducible human (N)-FLAG-α1β3γ2L-(GGS)3GK-1D4 $GABA_A$49, were grown on glass coverslips, and expression was induced by 0.1-2 μg/ml doxycycline for 14 to 28 hours depending on the level of current required. For pulling inside-out macro-patches, we used poly-L-lysine coated glass coverslips (Becton Dickinson, Franklin Lakes, NJ). Cells were also treated with kifunensine (5 μg/ml) at the time of induction.

Currents were recorded in either whole-cell or inside-out configuration of patch clamp as previously described50 using an Axopatch 200A amplifier (Molecular Devices, San Jose, CA). Ligands were applied via a quad-channel super-perfusion pipette coupled to a piezoelectric element that switched the super-perfusion solution in <1 ms as described previously51. Data were acquired using Clampex 8.2 (Molecular Devices, San Jose, CA). Data were acquired at either 10, 5 or 2 kHz and filtered at 5, 2 or 1 KHz respectively depending on the duration of the pulse, with longer the recording, the slower the data acquisition rate. Cells were continually perfused with a bath solution consisting of (in mM): 145 NaCl, 5 KCl, 10 HEPES, 2 $CaCl_2$, 1 $MgCl_2$ and 10 glucose, pH 7.4 (adjusted with NaOH). The pipette solution consisted of (in mM): 140 KCl, 10 HEPES, 1 EGTA, 2 $MgCl_2$ and 2 Mg-ATP, pH 7.3 (adjusted with KOH). For whole-cell recordings, the open pipette resistances ranged from 1.3 – 2.5 MΩ, cell capacitance ranged from 5 – 13 pF and series resistance ranged from 0.2 – 2.5 MΩ. Series resistances were electronically compensated by >85% with a lag of 10 μs. The liquid junction potential between the bath and pipette solution was −2 mV and was corrected post recordings. Cells and patches were voltage-clamped at −52 mV. For inside-out patches, the solutions were reversed, i.e., the pipettes were filled with the bath solution and the patches were perfused with the pipette solution. The pipette resistance for inside-out patches ranged from 4 – 6 MΩ. In all patch protocols, initially currents were repeatedly elicited with pulses of etomidate until stable currents were obtained before proceeding with the application of modulatory agents as described in the figure legend. For analysis 2 – 5 identical traces from the same patch were averaged, and the ones before the patch was stabilized were disregarded. The peak current amplitudes obtained with inside-out patches ranged between 7 – 44 pA.

Electrophysiology Data Analysis

Current traces were analyzed using Clampfit 9.0 (Molecular Devices, San Jose, CA). Statistical analysis (paired or unpaired Students *t* test) was done in Graphpad Prism 6 (Graphpad Software, La Jolla, CA). $P < 0.05$ was considered statistically significant. Data are shown as mean ± SD. Each *n* represents a different patch or cell. Current traces were normalized in Origin 6 for presentation. The enhancement data for Mb38 was fitted by nonlinear least squares in Igor Pro (Wavemetrics, Lake Oswego, OR).

Europe PMC Funders Author Manuscripts

Radioligand binding

The functionality of the receptors reconstituted in nanodiscs, in the presence or absence of Mb38 megabody, was assessed using radioligand binding assays. Modulation of 2 nM [^{3}H]flunitrazepam or [^{3}H]muscimol binding by varying concentrations of GABA or etomidate, respectively, was measured using WGA coated YSi scintillation proximity assay beads (SPA, PerkinElmer). Background binding was determined by displacement of [^{3}H]flunitrazepam or [^{3}H]muscimol with 100 μM diazepam or with 10 mM GABA respectively. Each reaction contained ~5 μg/ml purified receptor and 1 mg/ml SPA beads suspended in 10 mM HEPES pH7.5 and 100 mM NaCl. Data normalization, graph preparation and nonlinear least squares curve fitting to a single-site binding model were performed in Igor Pro 7 (WaveMetrics).

Europe PMC Funders Author Manuscripts

Extended Data

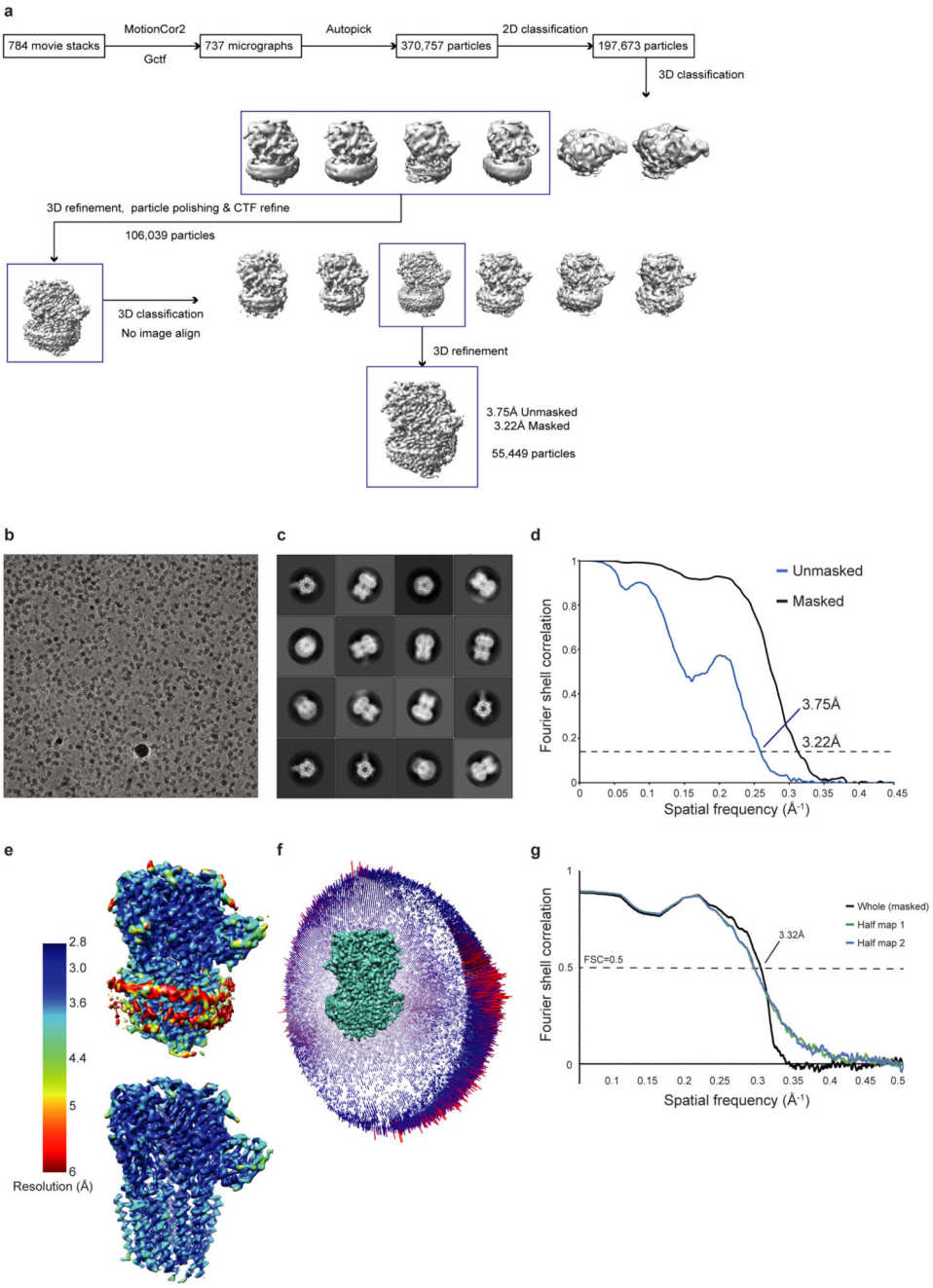

Extended Data Fig 1. Cryo-EM image processing procedure.

a. Overview of cryo-EM data collection and image processing procedure (see Methods). **b.** Representative micrograph of the α1β3γ2L-Mb38-nanodisc complex obtained using Falcon3 detector and VPP. **c.** Representative 2D class averages for downscaled data (box size of 240 Å). **d.** FSC curves for the reconstruction before and after applying a soft mask. **e.** The unsharpened map from refinement coloured by local resolution estimate (calculated

using MonoRes38) and shown at a low isosurface level to enable visualization of the nanodisc (left) and at a high isosurface level (right). **f.** Angular distribution histogram of particle used in calculating the final 3D reconstruction for the receptor assembly. **g.** FSC curves for cross-validation between maps and models: model versus summed map (black), model versus half map 1 (used in test refinement, green), model versus half map 2 (not used in test refinement, blue).

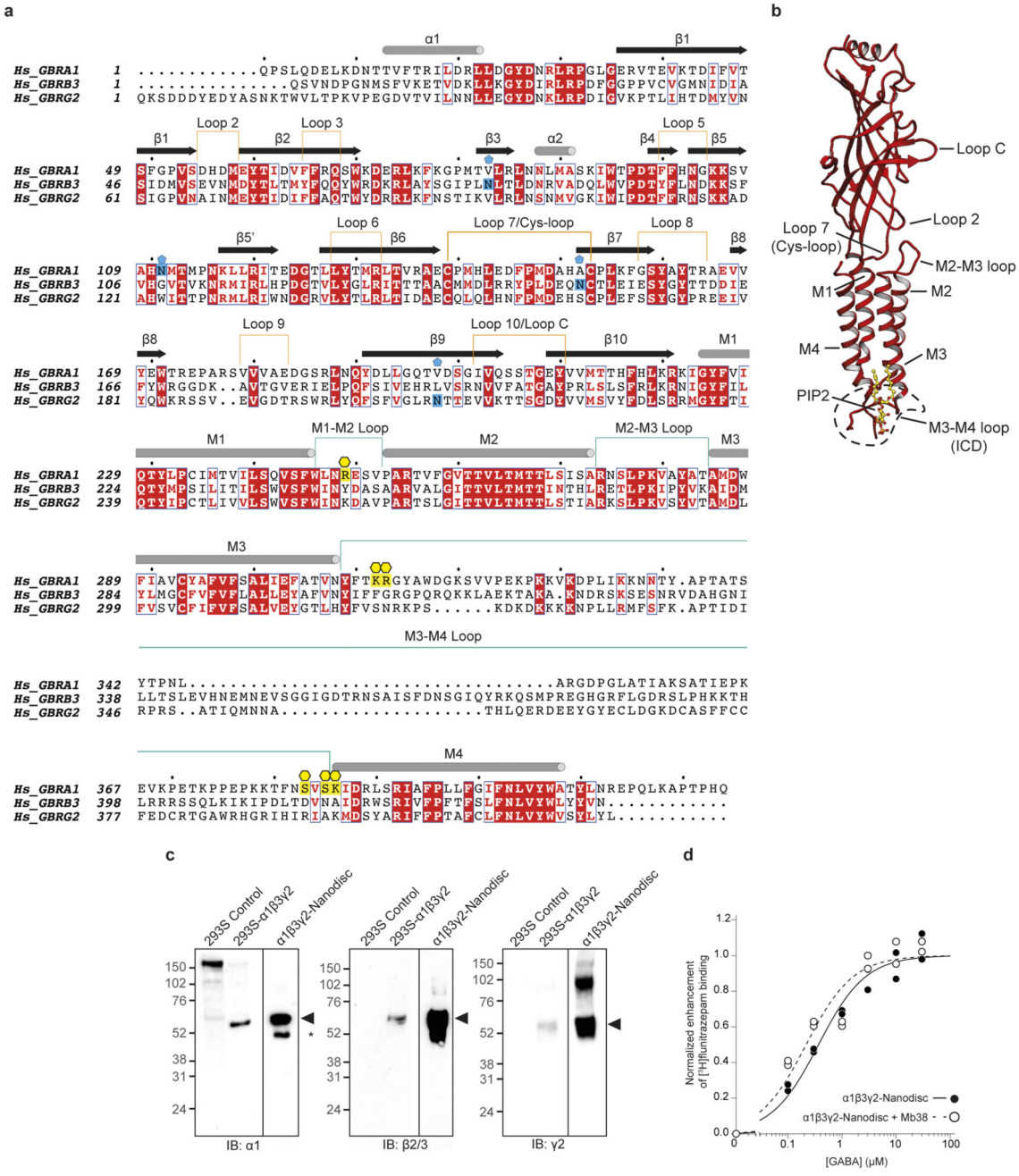

Extended Data Fig 2. Sequence alignment of GABA$_A$R α1, β3 and γ2 subunits, biochemical characterization and binding assays.

Europe PMC Funders Author Manuscripts

a. Alignment of wild-type $GABA_AR$ subunit sequences, where number one represents first residue of the mature protein. α-helices (grey cylinders), β-strands (black arrows) and associated loops are indicated. Glycosylation sites are indicated by blue pentagon and the associated subunit residue highlighted in blue. Residues identified as coordinating PIP2 binding are highlighted in yellow and indicated by yellow hexagons. The alignment graphic was prepared on the ESPript 3.0 server (http://espript.ibcp.fr/ESPript/ESPript/). **b.** Structure of a single α1 subunit. **c.** Western blot analysis of cell lysates from LMNG solubilized control HEK293 cells and α1β3γ2L $GABA_AR$ cells, and purified α1β3γ2L $GABA_ARs$ in nanodiscs. The arrowhead denotes the band corresponding to the full-length $GABA_AR$ subunits which migrates as a species of ~51-55 kDA. With the exception of the α1 subunit (which displays a small degree of proteolysis following reconstitution – denoted by asterisk), $GABA_AR$ subunits do not display apparent proteolysis during solubilization, purification and reconstitution. Western blots were repeated twice independently with similar results. **d.** GABA enhanced displaceable [^{3}H]flunitrazepam binding to purified receptors in a concentration–dependent manner in the presence or absence of Mb38. Points represent individual samples from two separate experiments.

Europe PMC Funders Author Manuscripts

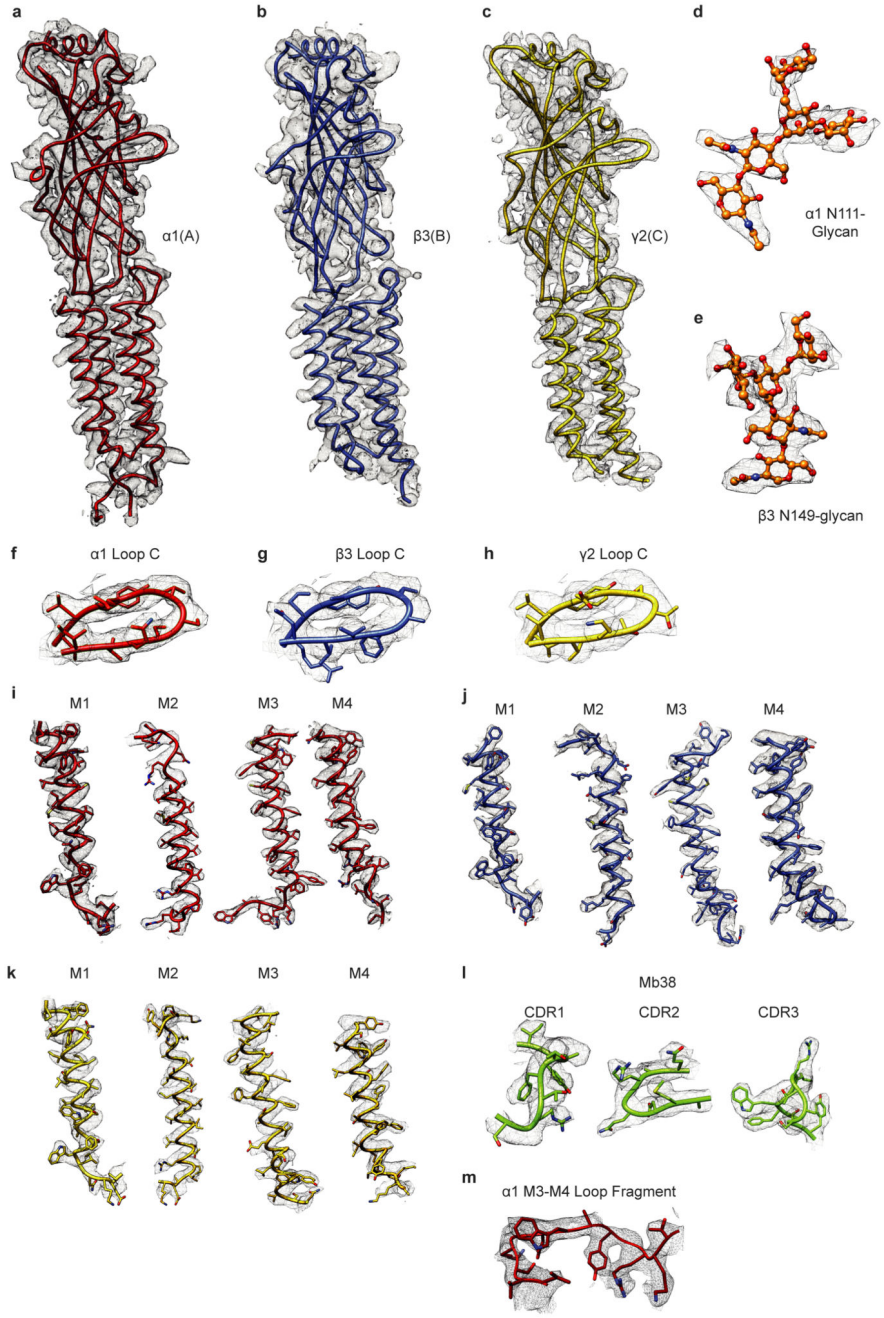

Extended Data Fig 3. α1β3γ2 model-map validation and EM density.

a-m. EM density segments for representative regions of each subunit and Mb38. Sharpened map contoured as detailed in Methods.

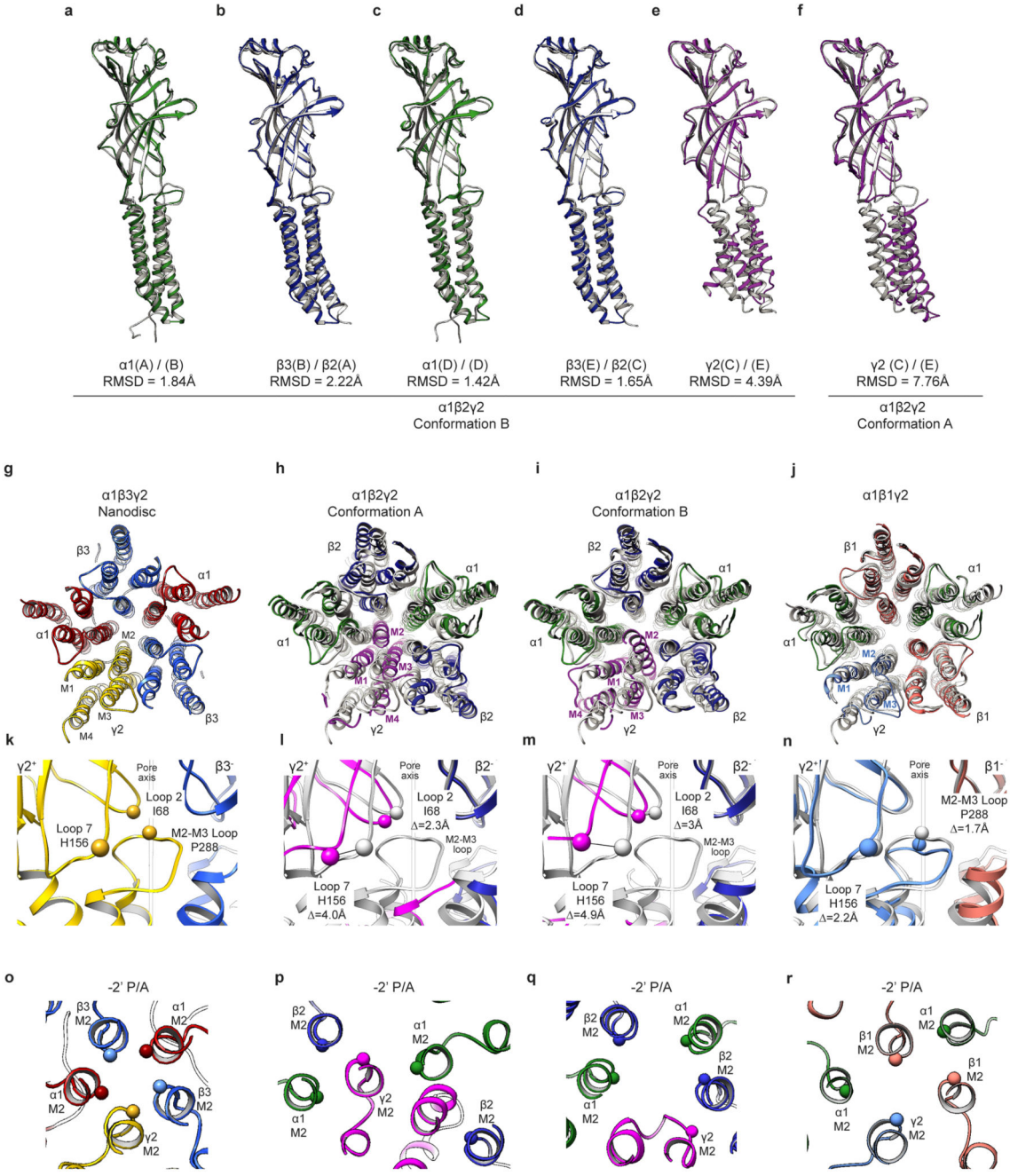

Extended Data Fig 4. Comparison of TMD architecture with α1β2γ2 and α1β1γ2 GABA$_A$R structures in detergent.

a-f. Superposition of subunit chains of α1β3γ2L GABA$_A$R (grey) onto equivalent chains of α1β2γ2 GABA$_A$R in DDM (Conformation B: PDB 6D6T) and the γ2 subunit of α1β2γ2 GABA$_A$R (Conformation A: PDB 6D6U). RMSD values are for Cα atoms over entire subunit. **g.** Overview of the TMD of α1β3γ2 in nanodisc. **h-j.** Superposition of TMD for α1β2γ2 GABA$_A$R conformation A (**h**), conformation B (**i**), α1β1γ2 GABA$_A$R (PDB: 6DW0 - **j**) and α1β3γ2-nanodisc complex (grey ribbon). TM helices of the γ2 subunit are

labelled. The TM helices of the γ2 show significant distortion in detergent-bound complexes. M4 helices in α1 and γ2 subunits were not modelled in the α1β1γ2 $GABA_AR$. **k-n.** Superposition of β^- subunits reveals conformational differences of $\gamma2^+$ subunit (α1β3γ2-nanodics complex in grey). Differences of distance (Å) between selected residue Cα atoms (spheres) is indicated by lines. Disruption of the γ2 TMD induces substantial displacement of loop 7, loop 2 and the M2-M3 loop at the ECD-TMD interface in the detergent bound α1β2γ2 structures (**l, m**), and to a lesser extend in α1β1γ2 $GABA_AR$ (**n**). **o-r.** Close up view of M2 helices at level of -2' proline/alanine residues (Cα atoms shown as sphere) in nanodisc (**o**) and detergent bound structures (**p-r**).

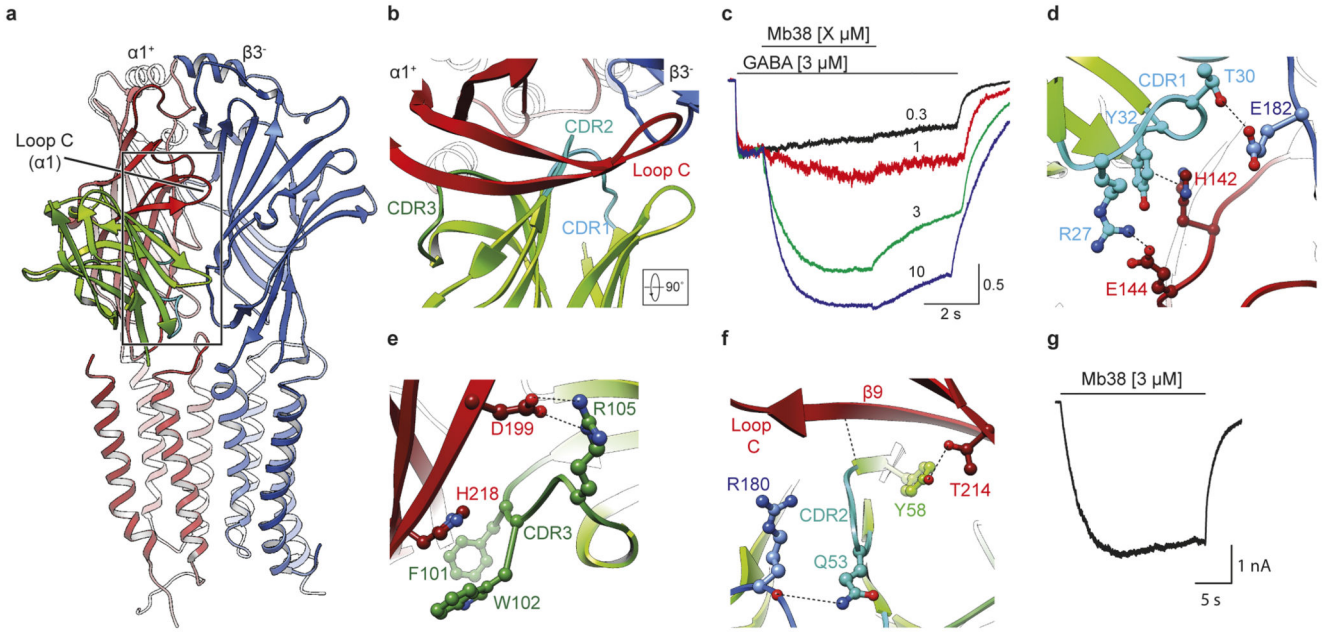

Extended Data Fig 5. Mb38 binding and function.

a. Side and **b.** top-down view of neighboring $\alpha1^+$ and $\beta3^-$ subunits bound to Mb38. **c.** Representative normalized current traces obtained in cells expressing α1β3γ2L receptor exposed to GABA (3 μM) alone or with varying concentrations of Mb38 (n = 3-6 cells), applied for 4 s. Currents were normalized to peak current amplitude obtained with GABA (3 μM) alone during the first 1s phase of the trace. The concentration of Mb38 is color-coded as indicated in the legend. **d-f.** Close-up view of the binding site when viewed approximately parallel to the plane of the membrane. CDR loops 1 (**d**), 2 (**e**) and 3 (**f**) of the Mb38 are colored in turquoise, teal and dark-green respectively and residues involved in interactions shown in ball-and-stick representation. Polar interactions are shown as dotted lines. **g**. Representative current trace obtained in cells expressing α1β3γ2L receptor exposed to 3 μM Mb38. Mb38 (3 μM) opened 16 ± 11 % (Mean ± SD; n = 5 cells) of the receptors gated by EC_{10} GABA alone (therefore ~2% of the total receptors expressed).

Europe PMC Funders Author Manuscripts

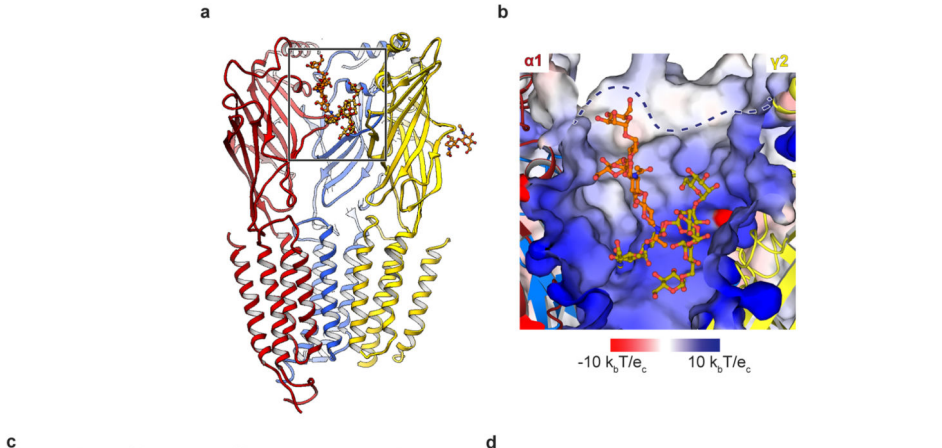

g

Interface	Interface area (Å²)	Calculated free energy ΔG (kcal mol⁻¹)	Tunnel bottleneck radius (Å)
β3-α1	3,119	-41.1	TMD – 1.42
β3-α1*	3,077	-43.1	TMD – 1.31
γ2-β3	2,858	-36.6	ECD – 1.45
α1-γ2	2,541	-30.3	ECD – 1.59
α1-β3	2,667	-31.1	ECD – 1.48
Mb38-α1	846	-6.0	-
Mb38-β3	241	-1.9	-

Extended Data Fig 6. Vestibular glycans and interface classes in the α1β3γ2L GABA$_A$R.
a. Side view of the receptor shows the position of vestibular α1 N-linked glycans. For clarity, the near α1 and β3 subunits have been removed. **b.** View across the extracellular vestibule reveals the stacking of α1 N-linked glycans. Receptor surface is coloured according to electrostatic surface potential and reveals an electropositive ring in middle portion of the ECD vestibule. **c-f.** Paired views of the interface between principle (+) and complementary (-) subunits viewed from the pore axis outwards (left) and open book view of each subunit when viewed from the receptor periphery (right). Residues involved in

forming interactions (defined using PDBePISA45) are colored according to the type of interaction and mapped onto the isosurface representation; polar – cyan, electrostatic/salt bridges – magenta and van der Waals – orange. Arrowheads reveal the openings of defined tunnels between adjacent subunits **g.** Calculated interfacial buried surface areas and solvation energy gain at complex formation (both calculated using PDBePISA44). The asterisk denotes the second β3 - α1 (chain E-chain A) interface in the pentameric assembly. Radii of tunnels, denoted by arrowhead in panel **c-f**, were also calculated (see Methods). Open arrowheads in panels **c, e** denotes cavities forming proposed anesthetic binding sites (as discussed in the text).

Europe PMC Funders Author Manuscripts

Europe PMC Funders Author Manuscripts

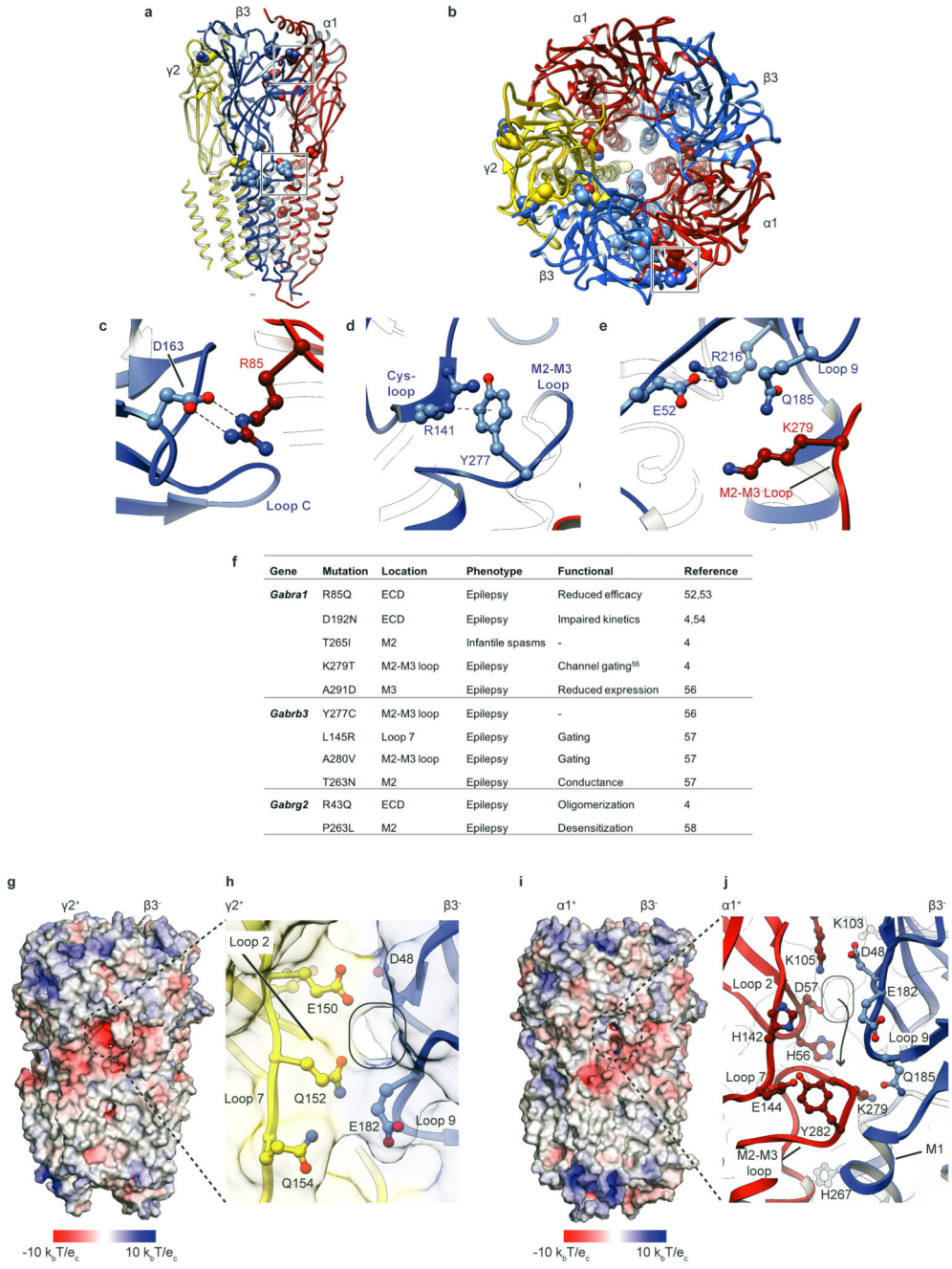

Gene	Mutation	Location	Phenotype	Functional	Reference
Gabra1	R85Q	ECD	Epilepsy	Reduced efficacy	52,53
	D192N	ECD	Epilepsy	Impaired kinetics	4,54
	T265I	M2	Infantile spasms	-	4
	K279T	M2-M3 loop	Epilepsy	Channel gating[55]	4
	A291D	M3	Epilepsy	Reduced expression	56
Gabrb3	Y277C	M2-M3 loop	Epilepsy	-	56
	L145R	Loop 7	Epilepsy	Gating	57
	A280V	M2-M3 loop	Epilepsy	Gating	57
	T263N	M2	Epilepsy	Conductance	57
Gabrg2	R43Q	ECD	Epilepsy	Oligomerization	4
	P263L	M2	Epilepsy	Desensitization	58

Extended Data Fig 7. Disease mutations associated with α1, β3 and γ2, lateral tunnels and fenestrations at the subunit interfaces.

a, b. Disease mutations associated with $GABA_A$ α1, β3 and γ2 subunits are mapped onto the structure and shown in sphere representation. The receptor is viewed parallel to the membrane plane (**a**) and from the extracellular aspect (**b**). Outlined boxes highlight position of mutations shown in the panels (**c-e**). **c-e.** Close up view of disease mutations associated with the α1 and β3 subunits. Polar interactions between residues are shown as dotted lines. **f.** Table summarising a number of disease mutations identified in genes for α1, β3 and γ2.

Functional effects as determined from experimental studies of channels properties are summarised. **g.** Exposed surface of the γ2-β3 subunit interface coloured according to electrostatic surface potential. **h.** Close up view of an electronegative fenestration formed at the γ2-β3 extracellular domain interface. The continuous tunnel leading from extracellular space to the receptor vestibule is outlined. **i.** Exposed surface of the α1-β3 subunit interface coloured according to electrostatic surface potential. **j**. Close-up view of the α1-β3 extracellular interface reveals an upper tunnel leading to the mid-portion of the ECD vestibule. A lower tunnel (denoted by arrow) opens into the upper aspect of the ion channel at the level of β3His267, a residue implicated in mediating the effects of propofol59.

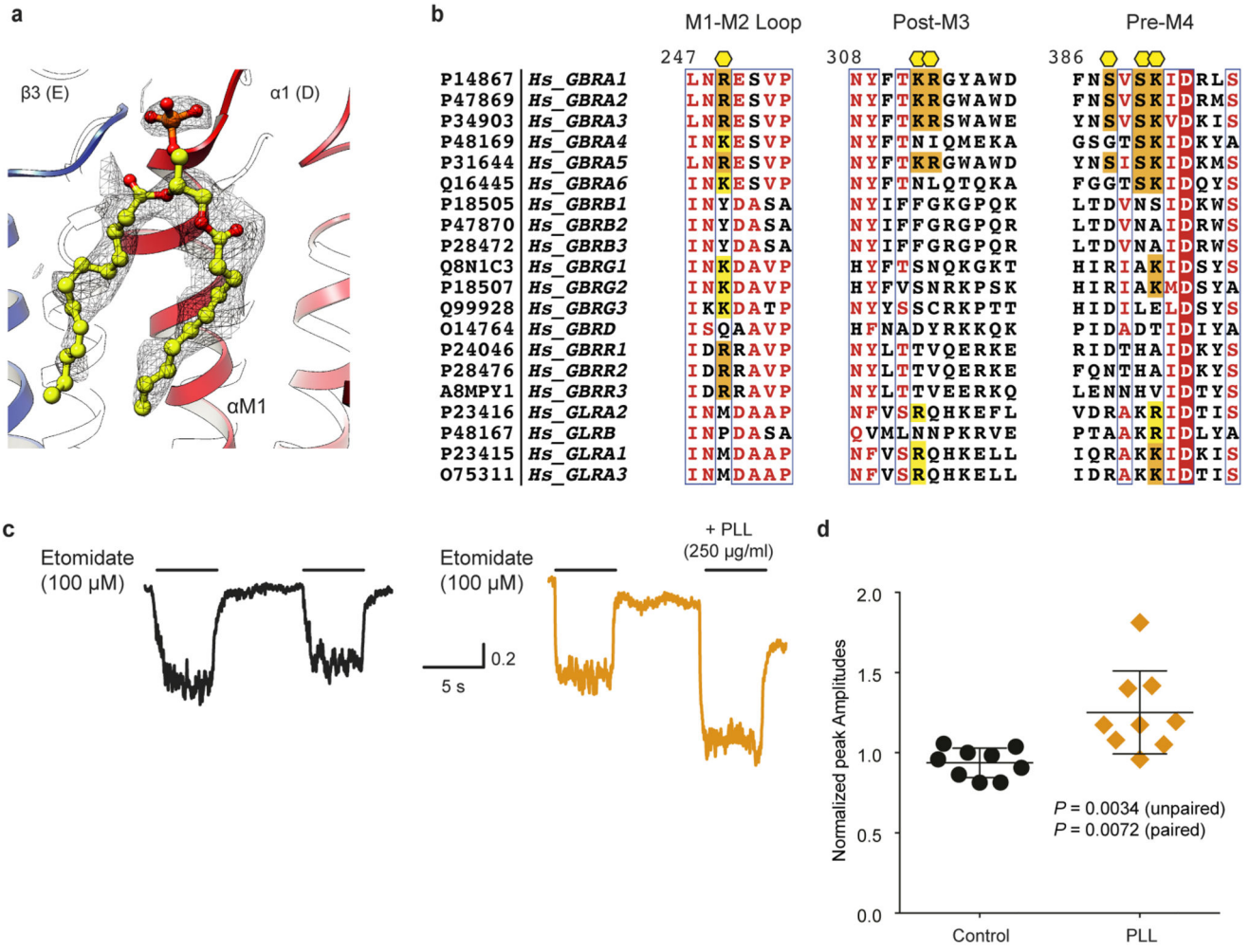

Extended Data Fig 8. Lipid binding sites and functional modulation of $GABA_AR$ by PIP2.

a. Well resolved density for POPC lipid moiety (yellow, ball-and-stick representation) at the extracellular aspect of the lipid nanodisc. EM density is shown in chicken wire representation and contoured around the lipids. **b.** Sequence alignment of $GABA_AR$ and GlyR subunits for PIP2 binding regions; the M1-M2 loop, post-M3 and pre-M4 segments. α1 residues forming hydrogen-bonds or salt-bridge interactions with PIP2 are identified by yellow hexagons, and those which are conserved amongst receptor subunits are highlighted

in orange (identical) and yellow (similar). The alignment graphic was prepared on the ESPript 3.0 server (http://espript.ibcp.fr/ESPript/ESPript/). **c.** Representative normalized current traces from the same patch, obtained in a two-pulse protocol, where inside-out patches were exposed to two 5 s etomidate (100μM) pulses 7.5 s apart. During the second pulse, etomidate was either applied alone or co-applied with PLL (250 μg/ml). Currents traces were normalized to the peak current amplitude obtained during the first etomidate pulse. **d.** Dot plot of peak current amplitudes obtained during the second pulse (co-application of PLL) normalized to the peak current amplitudes obtained with first pulse of etomidate (center value represents mean ± SD; n = 9 patches). Unpaired and paired Students *t* test (Two-tailed) values obtained are given in the figure.

Europe PMC Funders Author Manuscripts

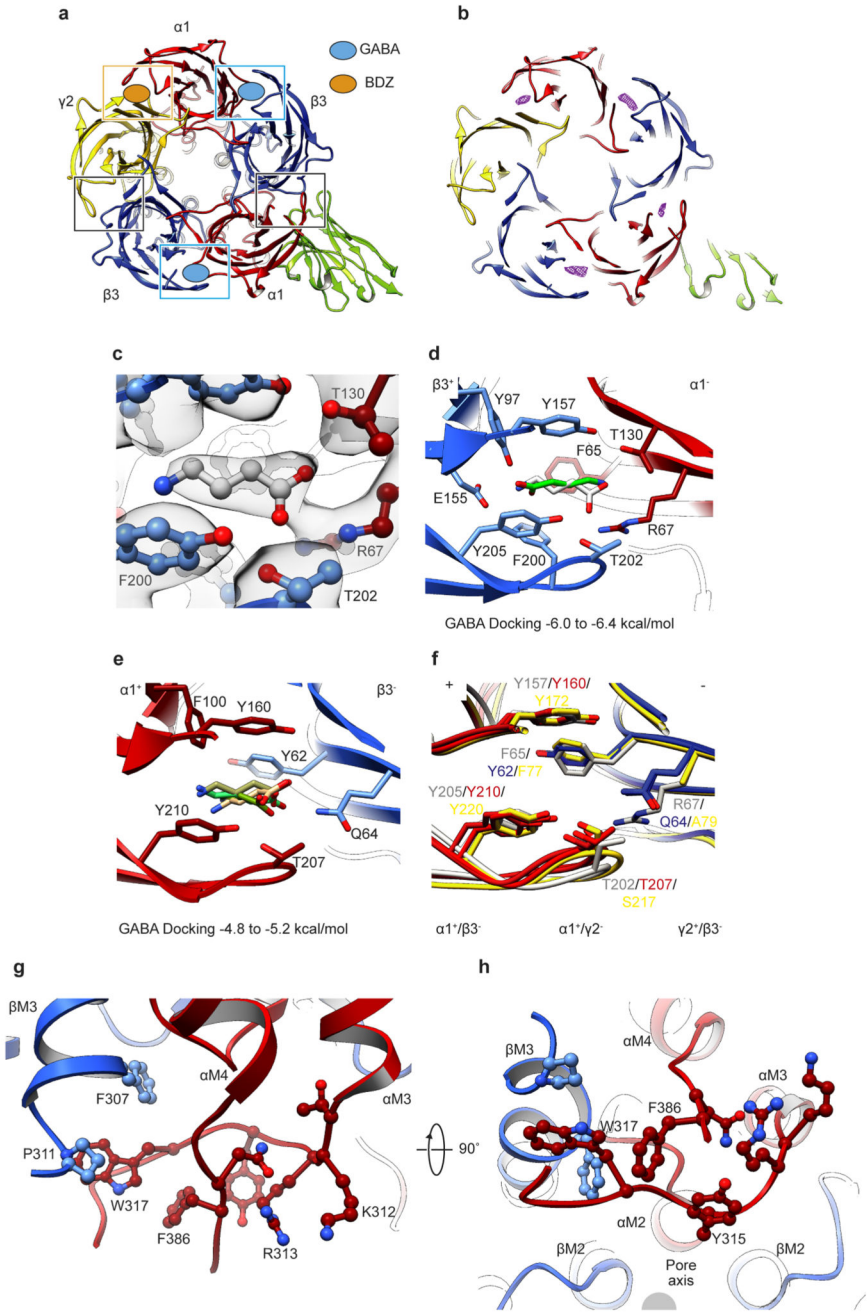

Extended Data Fig 9. Comparisons of agonist sites and analogous pockets at other subunit interfaces.

a. View of the receptor from across the synaptic cleft with the agonist binding sites highlighted. **b.** Cut-away view of **(a)** at the level of loops C, reveals EM density (shown as magenta chicken wire representation) at four inter-subunit pockets. **c.** EM density in the orthosteric binding pocket shown (grey surface representation). For comparison, the top binding pose for GABA is displayed in grey ball-and-stick representation. **d, e.** Overlay of GABA binding poses from molecular docking calculations at the β3-α1 (**d**) and α1-β3 (**e**)

binding pockets. The range of estimated free energies of binding (kcal/mol) is given. **f.** Comparison of the orthosteric binding pocket at the β3-α1 interface (grey), with the 3 unique interfaces observed in the α1β3γ2-Mb38 receptor (coloured as in **a.**) Superposition of the (-) subunit ECD reveals the relative movement of the (+) subunit ECD. **g, h.** Modelling of the intracellular end of M3 and M4 helices, contributing to the receptor intracellular domain, shown approximately parallel (**g**) and perpendicular (**h**) to the plane of the membrane.

Extended Data Table 1

Cryo-EM data collection, refinement and validation statistics.

	α1β3γ2-Mb38 Nanodisc (EMDB-4411) (PDB 6I53)
Data collection and processing	
Magnification	75,000
Voltage (kV)	300
Electron exposure (e–/Å^2)	30.84
Defocus range (μm)	-0.5 to -0.7
Pixel size (Å)	1.07
Symmetry imposed	C1
Initial particle images (no.)	370,757
Final particle images (no.)	55,559
Map resolution (Å)	3.22
FSC threshold	0.143
Refinement	
Map sharpening *B* factor (Å^2)	-68
Model composition	
Non-hydrogen atoms	15,366
Protein residues	1,821
Ligands	558
B factors (Å^2)	
Protein	156
Ligand	180
R.m.s. deviations	
Bond lengths (Å)	0.06
Bond angles (°)	0.801
Validation	
MolProbity score	1.43 (100th percentile)
Clashscore	3.53 (100th percentile)
Poor rotamers (%)	0
Ramachandran plot	
Favored (%)	95.8
Allowed (%)	4.2

	α1β3γ2-Mb38 Nanodisc (EMDB-4411) (PDB 6I53)
Disallowed (%)	0

Supplementary Material

Refer to Web version on PubMed Central for supplementary material.

Acknowledgments

We thank G. Cannone and S. Chen for EM support; J. Grimmett and T. Darling for computing support; L. Dong, T. Nakane and S. Scheres for advice on EM data processing; members of the Aricescu laboratory for assistance with EM data collection, discussions and comments on the manuscript. This work was supported by the UK Medical Research Council grants MR/L009609/1, MC_UP_1201/15 (A.R.A., D.L., S.M.) and MC_UP_A025_1013 (J.Z.); UK Biotechnology and Biological Sciences Research Council grant BB/M024709/1 (A.R.A., D.L.); Human Frontier Science Program grant RGP0065/2014 (A.R.A.); Cancer Research UK grant C20724/A14414 (T.M.); Swiss National Science Foundation fellowship 168735 (J.Z.). R.D., W.J.S and K.W.M. were supported by a grant from the National Institute for General Medical Sciences (GM 58448) and by the Department of Anesthesia, Critical Care and Pain Medicine, Massachusetts General Hospital. We thank INSTRUCT, part of the European Strategy Forum on Research Infrastructures and the Research Foundation-Flanders (FWO) for funding nanobody discovery and for a doctoral fellowship to T.U.

References

1. Sigel E, Steinmann ME. Structure, function, and modulation of $GABA_A$ receptors. J Biol Chem. 2012; 287:40224–40231. [PubMed: 23038269]
2. Olsen RW, Sieghart W. $GABA_A$ receptors: subtypes provide diversity of function and pharmacology. Neuropharmacology. 2009; 56:141–148. [PubMed: 18760291]
3. Braat S, Kooy RF. The $GABA_A$ Receptor as a Therapeutic Target for Neurodevelopmental Disorders. Neuron. 2015; 86:1119–1130. [PubMed: 26050032]
4. Macdonald RL, Kang J-Q, Gallagher MJ. Mutations in $GABA_A$ receptor subunits associated with genetic epilepsies. J Physiol (Lond.). 2010; 588:1861–1869. [PubMed: 20308251]
5. Fritschy JM, Mohler H. $GABA_A$-receptor heterogeneity in the adult rat brain: differential regional and cellular distribution of seven major subunits. J Comp Neurol. 1995; 359:154–194. [PubMed: 8557845]
6. Nguyen Q-A, Nicoll RA. The $GABA_A$ Receptor β; Subunit Is Required for Inhibitory Transmission. Neuron. 2018; :1–25. DOI: 10.1016/j.neuron.2018.03.046
7. Miller P, et al. Heteromeric $GABA_A$ receptor structures in positively-modulated active states. 2018; doi: 10.1101/338343
8. Phulera S, et al. Cryo-EM structure of the benzodiazepine-sensitive α1β1γ2S tri-heteromeric $GABA_A$ receptor in complex with GABA. Elife. 2018; 7:531.
9. Zhu S, et al. Structure of a human synaptic $GABA_A$ receptor. Nature. 2018; :1–22. DOI: 10.1038/s41586-018-0255-3
10. Miyazawa A, Fujiyoshi Y, Unwin N. Structure and gating mechanism of the acetylcholine receptor pore. Nature. 2003; 423:949–955. [PubMed: 12827192]
11. Unwin N. Refined structure of the nicotinic acetylcholine receptor at 4Å resolution. J Mol Biol. 2005; 346:967–989. [PubMed: 15701510]
12. Nemecz Á, Prevost MS, Menny A, Corringer P-J. Emerging Molecular Mechanisms of Signal Transduction in Pentameric Ligand-Gated Ion Channels. Neuron. 2016; 90:452–470. [PubMed: 27151638]

13. Dostalova Z, et al. Human α1β3γ2L gamma-aminobutyric acid type A receptors: High-level production and purification in a functional state. Protein Sci. 2014; 23:157–166. [PubMed: 24288268]
14. Masiulis S, Desai R, Uchański T, Serna Martin S, Laverty D, Karia D, Malinauskas T, Zivanov J, Pardon E, Kotecha A, Steyaert J, et al. $GABA_A$ receptor signalling mechanisms revealed by structural pharmacology. Nature. 2018
15. Gielen M, Thomas P, Smart TG. The desensitization gate of inhibitory Cys-loop receptors. Nat Commun. 2015; 6
16. Papke D, Grosman C. The role of intracellular linkers in gating and desensitization of human pentameric ligand-gated ion channels. J Neurosci. 2014; 34:7238–7252. [PubMed: 24849357]
17. Hille B, Dickson EJ, Kruse M, Vivas O, Suh B-C. Phosphoinositides regulate ion channels. Biochim Biophys Acta. 2015; 1851:844–856. [PubMed: 25241941]
18. Hansen SB, Tao X, MacKinnon R. Structural basis of PIP2 activation of the classical inward rectifier K+ channel Kir2.2. Nature. 2011; 477:495–498. [PubMed: 21874019]
19. Mennerick S, Taylor AA, Zorumski CF. Phosphatidylinositol 4,5-bisphosphate depletion fails to affect neurosteroid modulation of $GABA_A$ receptor function. Psychopharmacology (Berl.). 2014; 231:3493–3501. [PubMed: 24553581]
20. Amin J, Weiss DS. $GABA_A$ receptor needs two homologous domains of the beta-subunit for activation by GABA but not by pentobarbital. Nature. 1993; 366:565–569. [PubMed: 7504783]
21. Hibbs RE, Gouaux E. Principles of activation and permeation in an anion-selective Cys-loop receptor. Nature. 2011; 474:54–60. [PubMed: 21572436]
22. Miller PS, Aricescu AR. Crystal structure of a human $GABA_A$ receptor. Nature. 2014; 512:270–275. [PubMed: 24909990]
23. Laverty D, et al. Crystal structures of a $GABA_A$ receptor chimera reveal new endogenous neurosteroid-binding sites. Nat Struct Mol Biol. 2017; 24:977–985. [PubMed: 28967882]
24. Miller PS, et al. Structural basis for $GABA_A$ receptor potentiation by neurosteroids. Nat Struct Mol Biol. 2017; 24:986–992. [PubMed: 28991263]
25. Auerbach A, Akk G. Desensitization of mouse nicotinic acetylcholine receptor channels. A two-gate mechanism. J Gen Physiol. 1998; 112:181–197. [PubMed: 9689026]
26. Bali M, Akabas MH. The location of a closed channel gate in the $GABA_A$ receptor channel. J Gen Physiol. 2007; 129:145–159. [PubMed: 17227918]
27. Forman SA, Miller KW. Mapping General Anesthetic Sites in Heteromeric γ-Aminobutyric Acid Type A Receptors Reveals a Potential For Targeting Receptor Subtypes. Anesth Analg. 2016; 123:1263–1273. [PubMed: 27167687]
28. Li G-D, et al. Identification of a $GABA_A$ receptor anesthetic binding site at subunit interfaces by photolabeling with an etomidate analog. J Neurosci. 2006; 26:11599–11605. [PubMed: 17093081]
29. Jurd R, et al. General anesthetic actions in vivo strongly attenuated by a point mutation in the $GABA_A$ receptor β3 subunit. FASEB J. 2003; 17:250–252. [PubMed: 12475885]
30. Jayakar SS, et al. Positive and Negative Allosteric Modulation of an α1β3γ2 γ-Aminobutyric Acid Type A ($GABA_A$) Receptor by Binding to a Site in the Transmembrane Domain at the γ^+-β- Interface. J Biol Chem. 2015; 290:23432–23446. [PubMed: 26229099]
31. Tretter V, et al. Gephyrin, the enigmatic organizer at GABAergic synapses. Front Cell Neurosci. 2012; 6:23. [PubMed: 22615685]
32. Unwin N. Segregation of lipids near acetylcholine-receptor channels imaged by cryo-EM. IUCrJ. 2017; 4:393–399.
33. Ritchie, TK, , et al. Liposomes, Part F. Vol. 464. Elsevier; 2009. 211–231.
34. Javaheri A, et al. Helicobacter pylori adhesin HopQ engages in a virulence-enhancing interaction with human CEACAMs. Nat Microbiol. 2016; 2
35. Zheng SQ, et al. MotionCor2: anisotropic correction of beam-induced motion for improved cryo-electron microscopy. Nat Methods. 2017; 14:331–332. [PubMed: 28250466]
36. Zhang K. Gctf: Real-time CTF determination and correction. J Struct Biol. 2016; 193:1–12. [PubMed: 26592709]

37. Scheres SHW. A Bayesian view on cryo-EM structure determination. J Mol Biol. 2012; 415:406–418. [PubMed: 22100448]
38. Vilas JL, et al. MonoRes: Automatic and Accurate Estimation of Local Resolution for Electron Microscopy Maps. Structure. 2018; 26:337–344.e4. [PubMed: 29395788]
39. de la Rosa-Trevín JM, et al. Scipion: A software framework toward integration, reproducibility and validation in 3D electron microscopy. J Struct Biol. 2016; 195:93–99. [PubMed: 27108186]
40. Pettersen EF, et al. UCSF Chimera--a visualization system for exploratory research and analysis. J Comput Chem. 2004; 25:1605–1612. [PubMed: 15264254]
41. Emsley P, Lohkamp B, Scott WG, Cowtan K. Features and development of Coot. Acta Crystallogr D Biol Crystallogr. 2010; 66:486–501. [PubMed: 20383002]
42. Afonine PV, et al. Real-space refinement in PHENIX for cryo-EM and crystallography. Acta Crystallogr D Struct Biol. 2018; 74:531–544. [PubMed: 29872004]
43. Davis IW, et al. MolProbity: all-atom contacts and structure validation for proteins and nucleic acids. Nucleic Acids Res. 2007; 35:W375–83. [PubMed: 17452350]
44. Krissinel E, Henrick K. Inference of macromolecular assemblies from crystalline state. J Mol Biol. 2007; 372:774–797. [PubMed: 17681537]
45. Baker NA, Sept D, Joseph S, Holst MJ, McCammon JA. Electrostatics of nanosystems: application to microtubules and the ribosome. Proc Natl Acad Sci USA. 2001; 98:10037–10041. [PubMed: 11517324]
46. McNicholas S, Potterton E, Wilson KS, Noble MEM. Presenting your structures: the CCP4mg molecular-graphics software. Acta Crystallogr D Biol Crystallogr. 2011; 67:386–394. [PubMed: 21460457]
47. Jurcik A, et al. CAVER Analyst 2.0: Analysis and Visualization of Channels and Tunnels in Protein Structures and Molecular Dynamics Trajectories. Bioinformatics. 2018; 6:7597.
48. Trott O, Olson AJ. AutoDock Vina: improving the speed and accuracy of docking with a new scoring function, efficient optimization, and multithreading. J Comput Chem. 2010; 31:455–461. [PubMed: 19499576]
49. Dostalova Z, et al. High-level expression and purification of Cys-loop ligand-gated ion channels in a tetracycline-inducible stable mammalian cell line: GABAA and serotonin receptors. Protein Sci. 2010; 19:1728–1738. [PubMed: 20662008]
50. Desai R, et al. Contrasting actions of a convulsant barbiturate and its anticonvulsant enantiomer on the α1 β3 γ2L GABAA receptor account for their in vivo effects. J Physiol (Lond.). 2015; 593:4943–4961. [PubMed: 26378885]
51. Forman SA. A hydrophobic photolabel inhibits nicotinic acetylcholine receptors via open-channel block following a slow step. Biochemistry. 1999; 38:14559–14564. [PubMed: 10545178]
52. Yuan H, Low C-M, Moody OA, Jenkins A, Traynelis SF. Ionotropic GABA and Glutamate Receptor Mutations and Human Neurologic Diseases. Mol Pharmacol. 2015; 88:203–217. [PubMed: 25904555]
53. Carvill GL, et al. GABRA1 and STXBP1: novel genetic causes of Dravet syndrome. Neurology. 2014; 82:1245–1253. [PubMed: 24623842]
54. Lachance-Touchette P, et al. Novel α1 and γ2 $GABA_A$ receptor subunit mutations in families with idiopathic generalized epilepsy. Eur J Neurosci. 2011; 34:237–249. [PubMed: 21714819]
55. Kash TL, Jenkins A, Kelley JC, Trudell JR, Harrison NL. Coupling of agonist binding to channel gating in the $GABA_A$ receptor. Nature. 2003; 421:272–275. [PubMed: 12529644]
56. Epi4K Consortium. et al. De novo mutations in epileptic encephalopathies. Nature. 2013; 501:217–221. [PubMed: 23934111]
57. Hernandez CC, et al. $GABA_A$ Receptor Coupling Junction and Pore GABRB3 Mutations are Linked to Early-Onset Epileptic Encephalopathy. Sci Rep. 2017; 7
58. Hernandez CC, et al. Altered Channel Conductance States and Gating of $GABA_A$ Receptors by a Pore Mutation Linked to Dravet Syndrome. eNeuro. 2017; 4
59. Yip GMS, et al. A propofol binding site on mammalian $GABA_A$ receptors identified by photolabeling. Nat Chem Biol. 2013; 9:715–720. [PubMed: 24056400]

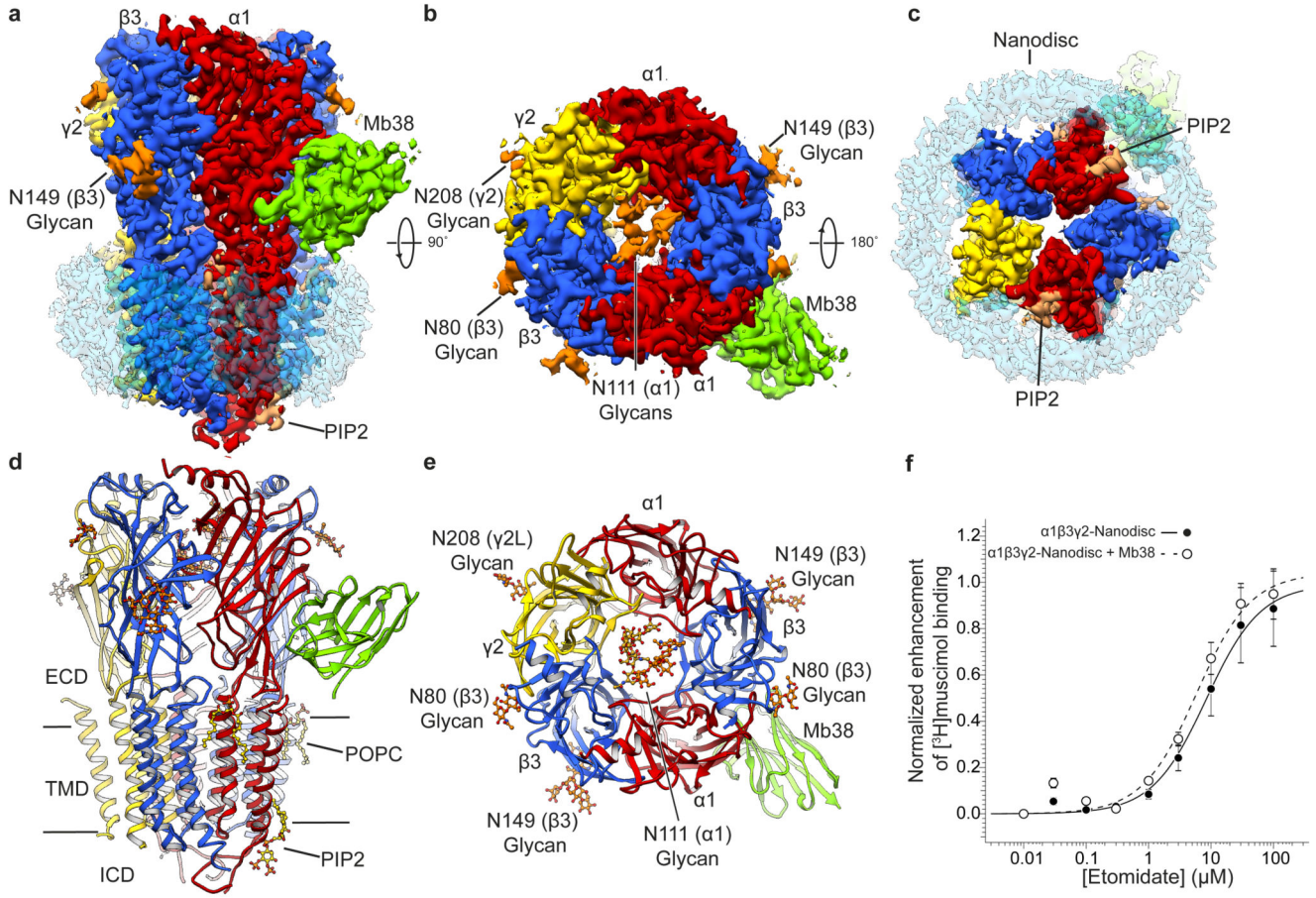

Figure 1. Architecture of full-length α1β3γ2L GABA$_A$R in lipid nanodiscs.

a-c. Side (**a**), top (**b**) and bottom (**c**) views of the sharpened cryo-EM map of α1β3γ2L GABA$_A$R-Mb38 complex in lipid nanodisc. Mb38 and glycans are colored green and orange, respectively. Density contributed by the nanodisc is colored in pale blue. **d, e.** Side (**d**) and top (**e**) views of atomic model of the α1β3γ2L GABA$_A$R in ribbon representation and glycans and lipids in ball-and-stick representation. Subunit coloring reflects that in (**a-c**). **f.** Etomidate enhancement of [^{3}H]muscimol binding at α1β3γ2L GABA$_A$R-nanodisc complexes in the presence or absence of Mb38. Each point represents average of at least 3-4 independent measurements and error bars correspond to one standard deviation, with the exception of points for 0.1 and 0.3 μM etomidate with Mb38 which represent two independent measurements.

Europe PMC Funders Author Manuscripts

Europe PMC Funders Author Manuscripts

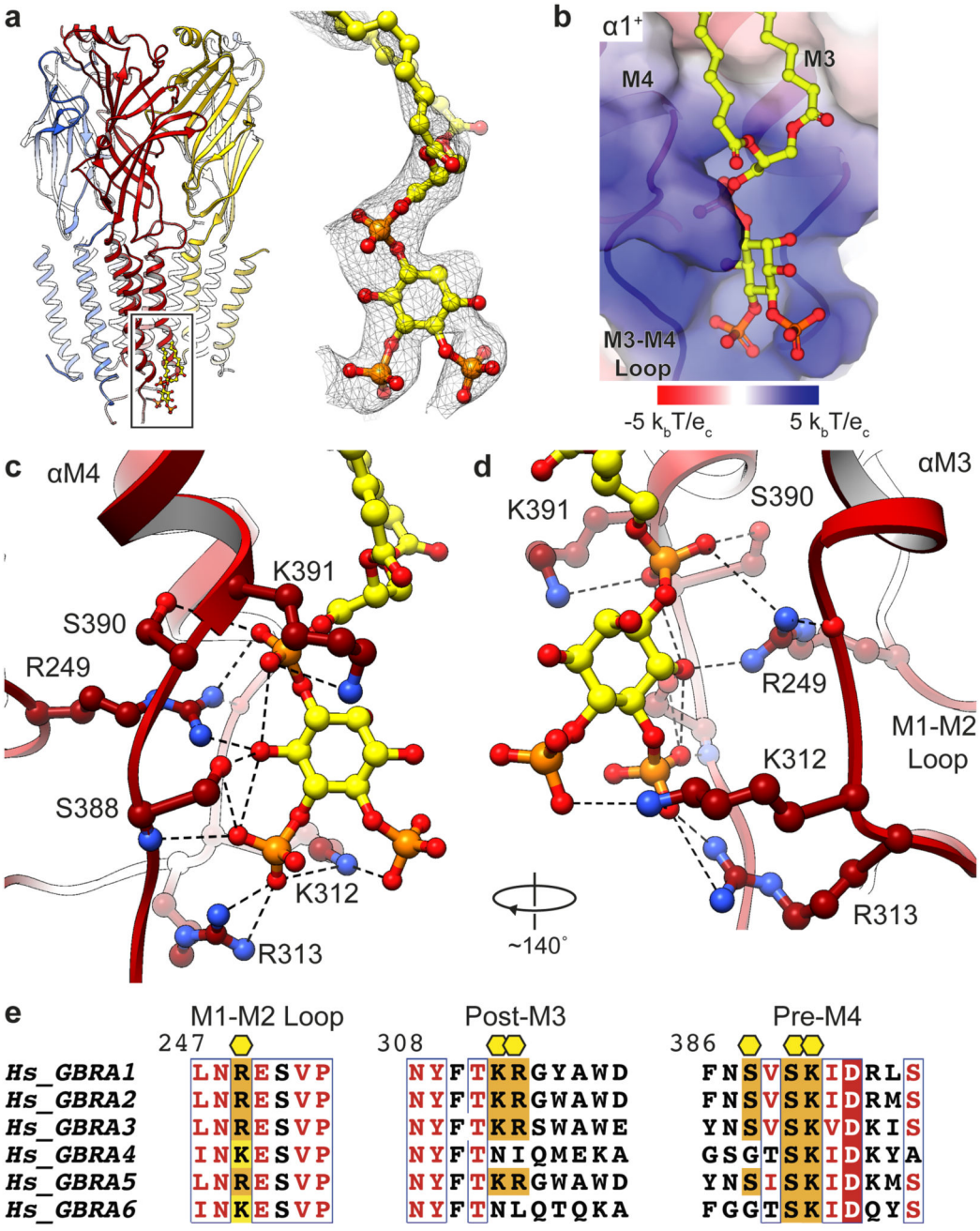

Figure 2. PIP2 binding sites in α1β3γ2L GABA$_A$R.

a. PIP2 bound at the base of α1 subunit TMDs. EM density map contoured around PIP2 (at α1 chain A binding site). **b.** Electrostatic surface potential shown at the 'cytosolic' end of α1 subunit and bound PIP2, shown in stick representation. **c, d.** PIP2 binding site when viewed approximately parallel to the plane of the membrane (**c**) and when rotated around the vertical axis (**d**). **e.** Sequence alignment of GABA$_A$R α-subunits for PIP2 binding regions. α1 residues forming hydrogen-bonds or salt-bridge interactions with PIP2 are identified by

yellow hexagons, and those which are conserved amongst α-receptor subunits are highlighted orange (identical) and yellow (similar).

Europe PMC Funders Author Manuscripts

Europe PMC Funders Author Manuscripts

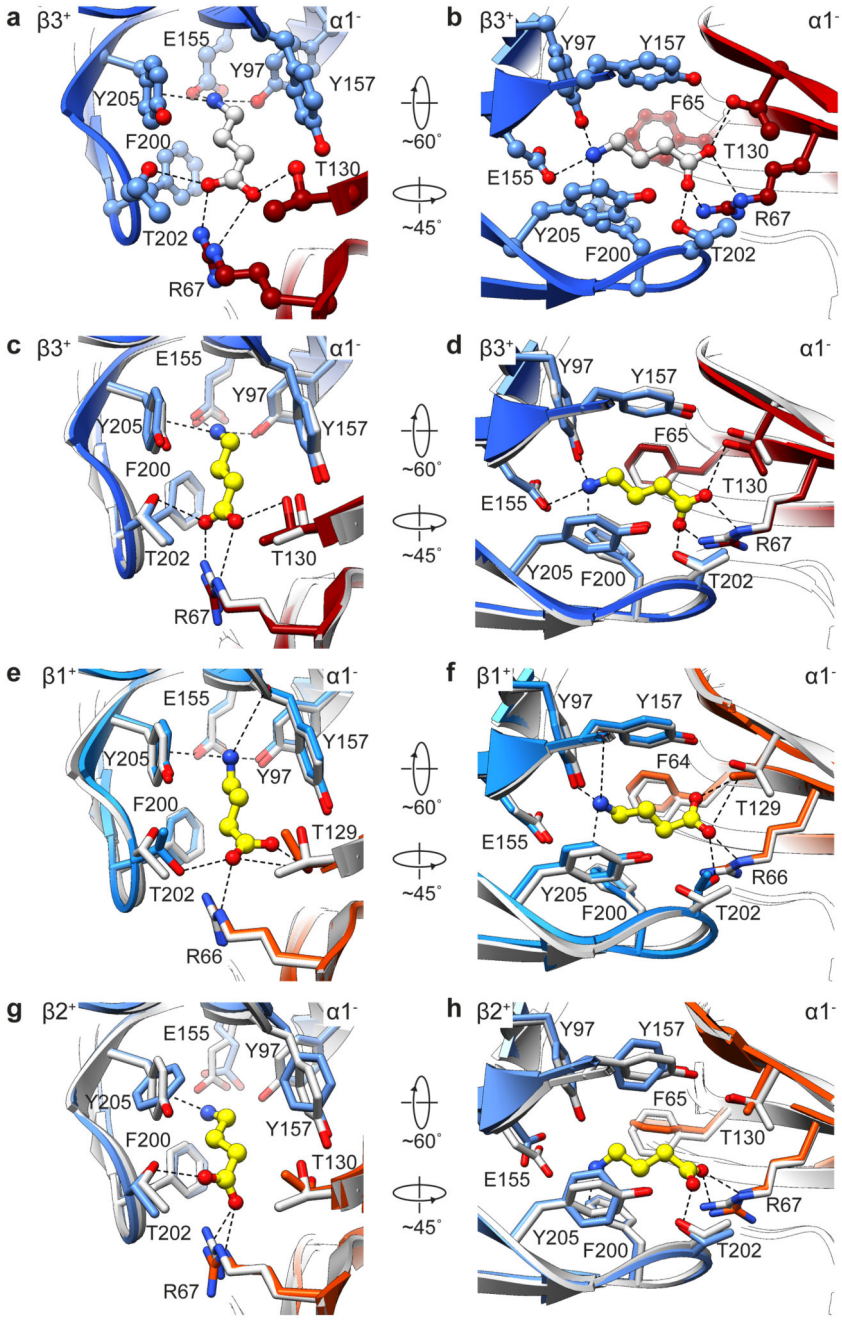

Figure 3. Neurotransmitter binding pocket and docked GABA.

a, b. Close-up view of the binding site when viewed approximately parallel to the plane of the membrane (**a**) and from the extracellular side (**b**). GABA, in its most energetically favored pose from computational docking analysis, is shown in grey ball-and-stick representation. Hydrogen bonds, salt bridges and cation-π interactions are shown as dotted lines. **c-h.** Superposition of the orthosteric binding site of α1β3γ2L (grey) with the alprazolam/GABA bound α1β3γ2L (**c, d.** PDB 6HUO) GABA-bound α1β1γ2 (**e, f.** PDB

6DW1) and α1β2γ2 (**g, h.** PDB 6D6U) $GABA_AR$ cryo-EM structures. Experimentally derived GABA (yellow ball-and-stick) poses and interactions (dotted lines) are shown.

Europe PMC Funders Author Manuscripts

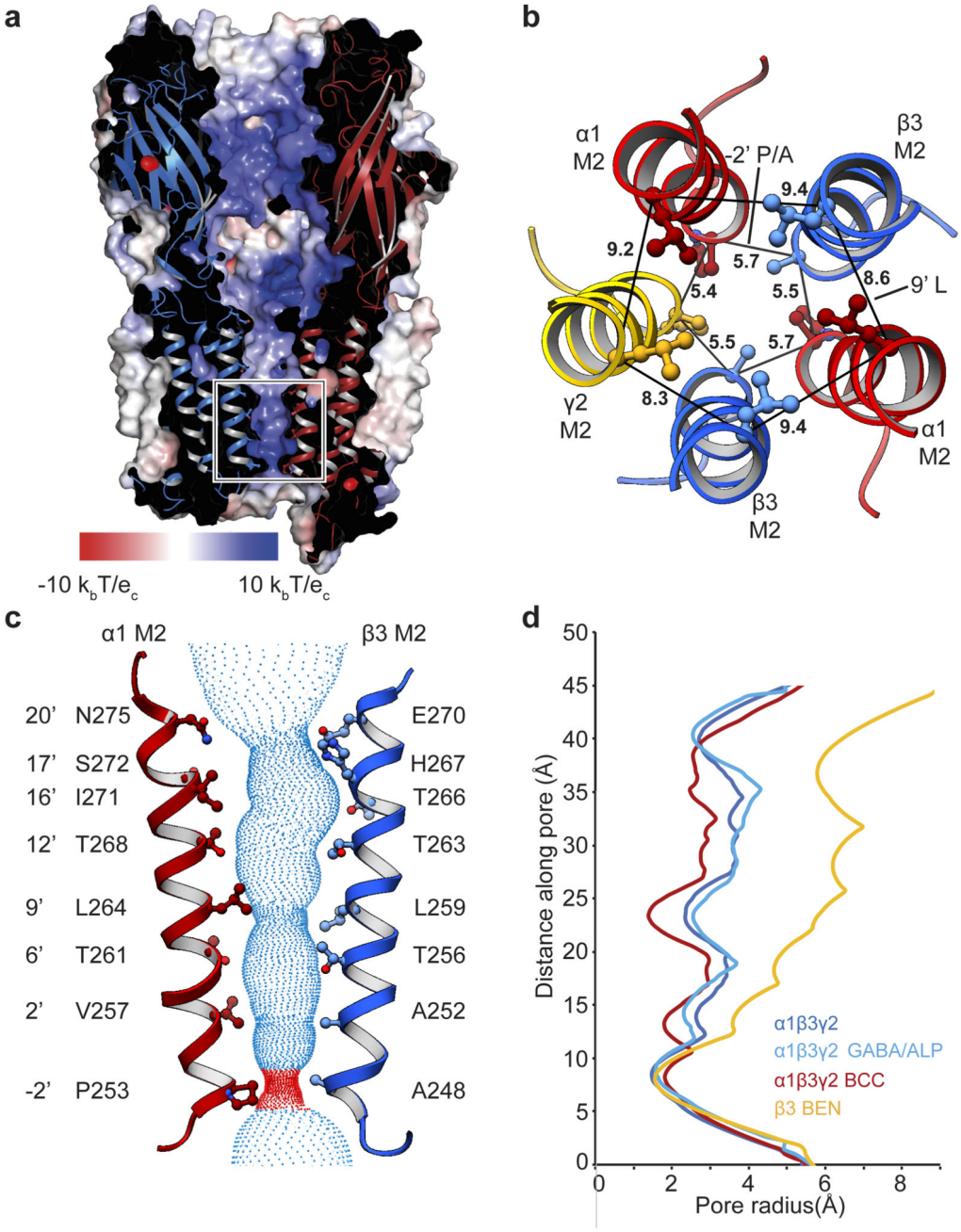

Figure 4. Conductance and permeation pore structure of the α1β3γ2L GABA$_A$R.

a. Cutaway of the receptor showing electrostatic surface potential along the ion conducting pathway. **b.** Asymmetry in the channel at the level of the activation and desensitization gates. -2' and 9' residues are shown in ball-and-stick representation. Distance between Cα of -2' and 9' residues are given in Å. **c.** M2 α-helices from opposing α1 and β3 subunits with sidechains shown for pore lining residues. Spheres represent the solvent accessible volume of the ion channel. Red spheres delimit the narrowest aspect of the channel. **d.** Profile of pore radius of the α1β3γ2L-Mb38 complex, alprazolam/GABA-bound α1β3γ2L (ALP;

PDB ID: 6HUO) and bicuculline-bound α1β3γ2L (BCC; PDB ID: 6HUK) and the benzamidine-bound β3 $GABA_A$ (BEN; PDB ID: 4COF).

Europe PMC Funders Author Manuscripts

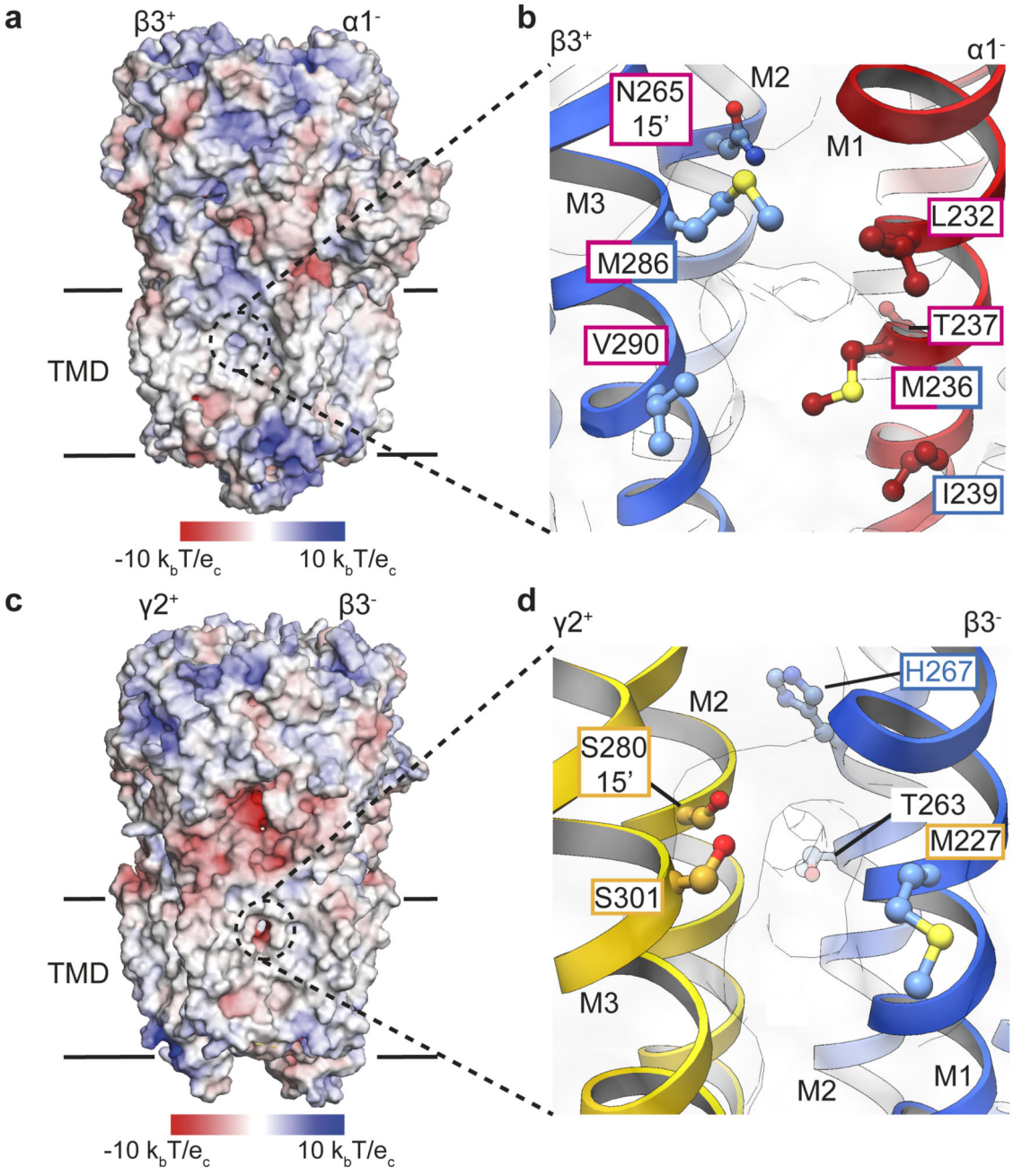

Figure 5. Anesthetic binding sites in the α1β3γ2L GABA$_A$R TMD

a. Exposed surface of the β3-α1 subunit interface coloured according to electrostatic surface potential. **b.** Close up view of a cavity formed at the transmembrane β-α interface. Residues identified in photolabeling studies with etomidate and propofol derivates are outlined in magenta and blue respectively. **c.** Exposed surface of the γ2-β3 subunit interface coloured according to electrostatic surface potential. **d.** Close up view of a cavity formed at the

transmembrane γ-β interface. Residues identified in photolabeling studies with propofol and barbiturate derivates are outlined in blue and orange respectively.

Europe PMC Funders Author Manuscripts